TUHH
Institut für
Mehrphasenströmungen

Master Thesis

Design and Characterization of a 3D-Printed Jet Loop Reactor with Optimized Flow Conditions for Enhanced Mass Transfer

Felix Kexel

First Examiner:	Prof. Dr.-Ing. Michael Schlüter
Second Examiner:	Prof. Dr. Andreas Liese
Tutor:	Nicolai Szeliga, M. Sc

Hamburg, September 2018 - March 2019

Eidesstattliche Erklärung

Hiermit versichere ich, dass ich die vorliegende Arbeit selbstständig verfasst und keine anderen als die angegebenen Quellen und Hilfsmittel benutzt habe, dass alle Ausführungen, die anderen Schriften wörtlich und sinngemäß entnommen wurden, kenntlich gemacht sind und dass die Arbeit in gleicher oder ähnlicher Fassung noch nicht Bestandteil einer Studien- oder Prüfungsleistung war.

Hamburg, den _____

_____

Unterschrift

Table of Content

List of Figures

List of Tables

List of Symbols

Latin Letters		
Symbol	***Property***	***Unit***
$\boldsymbol{a}$	Specific Area	m^{-1}
$\boldsymbol{A}$	Area	m^2
$\boldsymbol{C}$	Chord length	m
$\boldsymbol{C_X}$	Constant value X	-
$\boldsymbol{c_i}$	Concentration of component i	$mg \cdot L^{-1}$
$\boldsymbol{D}$	Diffusion	$m^2 \cdot s^{-1}$
$\boldsymbol{d}$	Diameter	m
$\boldsymbol{E}$	Energy flux	$kJ \cdot s^{-1}$
$\boldsymbol{e}$	Gassing tube length	mm
$\boldsymbol{g}$	Acceleration of gravity	$m \cdot s^{-2}$
$\boldsymbol{h}$	Height	m
$\boldsymbol{l}$	Length	m
$\boldsymbol{\dot{m}}$	Mass flux density	$kg \cdot s^{-1} \cdot m^{-2}$
$\boldsymbol{M}$	Molar mass	$g \cdot mol^{-1}$
$\boldsymbol{\dot{M}}$	Mass flux	$kg \cdot s^{-1}$
$\boldsymbol{\dot{n}}$	Mole flux density	$mol \cdot s^{-1} \cdot m^{-2}$
$\boldsymbol{\dot{N}}$	Molar flux	$mol \cdot s^{-1}$
$\boldsymbol{P}$	Power	kW
$\boldsymbol{p}$	Major	m

Symbol	***Property***	***Unit***
$\dot{\boldsymbol{q}}$	Heat conduction	$W \cdot m^{-2}$
$\boldsymbol{r}$	Radius	m
$\boldsymbol{R}$	Radius	m
$\boldsymbol{S}$	Surface	m^2
$\boldsymbol{s}$	Minor	m
$\boldsymbol{t}$	Time	s
$\boldsymbol{V}$	Volume	m^3
$\dot{\boldsymbol{V}}$	Volume flux	$m^3 \cdot s^{-1}$
$\boldsymbol{u, v, w}$	Velocity	$m \cdot s^{-1}$
$\boldsymbol{x}$	Spatial dimension	-
$\boldsymbol{y}$	Spatial dimension	-
$\boldsymbol{z}$	Spatial dimension	-

Greek Letters		
Symbol	***Property***	***Unit***
β_i	Mass transfer coefficient of i	$m \cdot s^{-1}$
δ	Boundary layer	m
Δ	Delta	-
ε	Hold-Up	%
ζ	Drag coefficient	-
η	dynamic viscosity	$Pa \cdot s$
ν	kinematic viscosity	$m^2 \cdot s^{-1}$
ρ	Density	$kg \cdot m^{-3}$
σ	Surface tension	$N \cdot m^{-1}$
τ	Stress tensor	MPa
φ	Void fraction	%

Indices & Exponents	
Symbol	***Notation***
0	Starting Value
10	Mean chord length
A2	A2-Photonics
D	Draft tube
d	Drag
DP	Deflection plate
E	Largest bubble
g	Gaseous
g,0	Superficial gas
GT	Gassing Tube
i	Species i
j	Species j
kin	Kinetic
L	Liquid
Loh	Constant value Lohrengel
N	Nozzle
R	Reactor
s	Swarm

Symbol	***Notation***
sa	Sauter
tot	Total
x	Variable
a	Correlation Parameter
b	Correlation Parameter
β	Correlation Parameter
γ	Correlation Parameter
κ	Correlation Parameter
ζ	Correlation Parameter
*	Saturation
∞	Bulk phase
→	Vector

Notation	*Equation*
Eötvös	$Eo = Bo = \frac{l^3 \cdot \Delta\rho \cdot g}{\sigma}$
Froude	$Fr = \frac{w}{\sqrt{g \cdot l}}$
Galilei	$Ga = \frac{l^3 \cdot g}{\nu^2}$
Morton	$Mo = \frac{\nu^4 \cdot g \cdot \Delta\rho}{\rho_L^2 \sigma^3}$
Sherwood	$Sh = \frac{l \cdot \beta_i}{D_{i,j}}$
Sherwood, industrial	$Sh_{ind} = \frac{d_R^2 \cdot \beta_L a}{D_{i,j}}$
Reynolds	$Re = \frac{u \cdot l}{\nu}$
Schmidt	$Sc = \frac{\nu}{D_{i,j}}$

Acronyms

Acronym	*Notation*
BMBF	Federal Ministry of Education and Research
JLR	Jet loop reactor
PMMA	Poly-(methyl)-methacrylate
SLS	Selective laser sintering
SLA	Stereolithography

Abstract

With the aim to achieve an enhanced mass transfer performance by applying additive manufacturing methods, a transparent jet loop reactor is designed and characterized. The reactor is built from acrylic glass, with an experimental draft tube to reactor diameter ratio of 0.71. In order to optimize the flow conditions, the edges of the draft tube are modeled as drop shaped widenings based on empirical observations and the work of *H. Blenke* [Ble71]. Simultaneously, creating a benchmark system, a cylindrical draft tube with sharp edges is designed and compared against.

The reactor performance is characterized by determining the overall gas hold-up, the bubble properties and the volume specific liquid-phase mass transfer coefficient in a water-air system. Though the flow optimization results in an overall increase in the gas holdup, it also causes an increase in the mean bubble size, yielding lower interfacial areas. Therefore, the volume specific mass transfer is not significantly increased by the flow optimized draft tube. Contrarily, for medium gassing rates, it tends to slightly decrease, due to the smaller interfacial area. Overall values of the volume specific mass transfer, obtained by the dynamic measurement method, are within a range of $\beta_L a = 50 - 90\ h^{-1}$. These results are confirmed by stationary measurements. The measured data is compared to correlations from literature, which are then refitted to better match the measurement results.

The results show that the use of a 3D-printed flow optimized draft tube is useful, if a chemical reaction is consuming a valuable gas as recirculation within the loop is intensified. A significant effect of the flow optimization on the mass transfer is not measurable, but the influence of the energy dissipation is reduced, which might reduce the overall energy consumption in the flow optimized reactor system.

1 Motivation

Increasing energy costs, growing demands for chemical products, rising environmental concerns and global competition are forcing the chemical, biochemical and pharmaceutical industry to constantly improve their production methods. Especially the parameter sustainability is emphasized throughout the scientific community and the general population, resulting in a growing demand for new production methods based on biological processes. As the chemical industry is just at the beginning of the implementation of such processes and the biotechnology sector is constantly growing, the *BMBF innovation alliance protP.S.I* is aiming for the application of biologically based processes in the field of fine chemicals and the investigation of pressure as a process parameter. The utilization of pressure allows shifting the chemical balance towards the strived product and therefore, provides a large potential for increasing the process efficiency and sustainability by connecting classical chemistry with modern biotechnology on an industrial scale.

One goal of the innovation alliance is the development of an enzymatic oxidation process, working under elevated pressure. As higher pressure results in a higher saturation concentration for oxygen in water, a reaction under high pressure has the potential to improve the yield of many enzymatic reactions. Since enzymes are vulnerable to shear stress, caused by bubbly flows, the enrichment of water with oxygen is conducted in a preliminary process step. The desired gassing unit must provide a good oxygen transfer and volume flow rate on one side, but also must be high pressure resistant and cost-efficient. By producing large interfacial areas, containing no moving parts in need of driving shafts and having a high H/D-ratio, a jet loop reactor is combining all requirements and can be safely operated at elevated pressures.

The aim of this thesis is the design, commissioning and characterization of a prototype gassing unit in the form of a jet loop reactor, using additive manufacturing methods for the improvement of the mass transfer performance. Therefore, two different designs of draft tubes are compared regarding the mass transfer performance.

2 Theoretical Background

In this chapter the necessary theories and equations, this thesis is based on, will be displayed and explained. The focus will be on the equation needed for the design and characterization of a jet loop reactor. Therefore, a short overview about Jet loop reactors is provided, the typical attributes of the JLR are explained and the fundamentals of mass transport are explained.

2.1 Fundamentals of Fluid Dynamics

The basic equations of fluid mechanics can be derived from the commonly known conservatory equations of mass, momentum and energy. The conservatory equation of mass, the continuity equation

$$\frac{\partial \rho}{\partial t} + \nabla \cdot (\rho \cdot \vec{v}) = 0 \tag{2.1}$$

can be derived, by making use of the nabla operator ∇, the velocity vector $\vec{v}$, the density ρ and the time t. The continuity equation states that the temporal change of mass within a finite volume must equal the entering and leaving mass flow. In case of an incompressible fluid the continuity equation can be simplified, resulting in

$$\nabla \cdot \vec{v} = 0 \tag{2.2}.$$

The continuity is an important measure for the design of the jet loop reactor in this thesis. [Oer15]

The conservation of momentum

$$\frac{\partial \rho \vec{v}}{\partial t} = -\nabla(\rho \vec{v}\vec{v}) - \nabla \vec{\tau} - \nabla p + \rho \vec{g} \tag{2.3}$$

states that the temporal change of momentum in a finite volume must be equal to the acting forces. With g representing the volume forces and τ the stress tensor, defined as a function of velocity and substance properties.

In case of an incompressible and Newtonian fluid a simplified equation, the Navier-Stokes equation

$$\rho \frac{\partial \vec{v}}{\partial t} = -\rho(\vec{v} \cdot \nabla)\vec{v} + \eta\nabla^2\vec{v} - \nabla p + \rho\vec{g} \qquad (2.4),$$

can be derived, with η as the dynamic viscosity. [Pas04]

As well as the conservation of mass and momentum, the conservation of energy must be considered. It states that the temporal change of internal and kinetic energy within a finite volume must be equal to all acting energies. The conservation of energy can be written as

$$\begin{aligned} &\frac{\partial}{\partial t}\left(\frac{1}{2}\rho\vec{v}^2 + \rho u\right) = -\nabla\left(\frac{1}{2}\rho\vec{v}^2 + \rho u\right)\vec{v} \\ &-\nabla \cdot \vec{q} - (\nabla \cdot p\vec{v}) - (\nabla \cdot [\vec{\tau} \cdot \vec{v}]) + \rho(\vec{v} \cdot \vec{g}) \end{aligned} \qquad (2.5),$$

with u as a velocity and q representing the heat conduction. The terms on the right represent the convective transport, the conduction, the work by pressure, the work by friction and the work by gravity. [Pas04]

Besides the governing equations of fluid mechanics mentioned above, dimensionless quantities are of great importance for this thesis. In the following the Archimedes, Bond, Froude, Galileo, Sherwood, Reynolds and Schmidt numbers will be displayed.

The Bond or Eötvös number is a dimensionless quantity in fluid mechanics and is representing the ratio of gravitational to surface tension forces and is defined by

$$Bo = Eo = \frac{l^3 \cdot \Delta\rho \cdot g}{\sigma} \qquad (2.7),$$

with σ representing the surface tension. [Vdi13a]

The Froude number is describing the ratio of the inertia forces and gravitational forces within a hydrodynamic system and is calculated by

$$Fr = \frac{w}{\sqrt{g \cdot l}} \quad (2.8),$$

considering the velocity w in the observed direction. [Vdi13a]

The Galilei number

$$Ga = \frac{l^3 \cdot g}{\nu^2} \quad (2.9)$$

is used in fluid dynamics for describing the ratio of gravitational and friction forces. [Vdi13a]

The Morton number characterizes dispersed two-phase flows

$$Mo = \frac{\nu^4 \cdot g \cdot \Delta\rho}{\rho_L^2 \sigma^3} \quad (2.10)$$

setting viscos forces and surface tension into ratio. Per definition, the Morton number only depends on the substance properties of the gas and the liquid. [Vdi13a]

The Sherwood number is an important dimensionless quantity used for mass transfer operations. It represents the ratio of convective and diffusive mass transport. It takes the mass transfer coefficient β and the diffusion coefficient $D_{i,j}$ into account. The Sherwood number

$$Sh = \frac{l \cdot \beta}{D_{i,j}} \quad (2.11)$$

is of greater interest at empirical correlations for the mass transfer at bubbles. [Vdi13a]

In literature many correlations, especially for jet loop reactors are used, which are using a slightly modified Sherwood number

$$Sh_{ind} = \frac{d_R^2 \cdot \beta_L a}{D_{i,j}} \quad (2.11),$$

containing the volume specific mass transfer coefficient $\beta_L a$ and as the characteristic length the reactor diameter d_R. In the following this Sherwood number is referred to as the industrial Sherwood number. [Vdi13a]

The Reynolds number

$$Re = \frac{u \cdot l}{\nu} \quad (2.11)$$

is an important quantity usually used for the prediction of flow patterns. It sets the inertia force and viscos force into ratio. [Vdi13a]

The Schmidt number

$$Sc = \frac{\nu}{D_{AB}} \quad (2.12)$$

represents the ratio of momentum diffusivity and mass diffusivity. [VDI13a]

2.2 Jet Loop Reactors

In the chemical and biochemical industries reactions often involve a mass transfer between a gas and a liquid or the adsorption of a gas into a liquid. Typical gas-liquid contactors are stirred tank reactors (STR), aerated tanks, bubble columns and the investigated jet loop reactors. [Loh90]

In general, a loop reactor can be split into an upstream and a downstream zone. Those zones can be established in two ways. Either by a draft tube inside the reactor tube, resulting in an inner circulation, or by a zone at the outside of the reactor, called external circulation. A system with inner circulation consists of three main parts, the reactor pipe, a draft tube and a momentum generator. The momentum generator, often a propeller or a pump, circulates the content around the draft tube. The inner flow superimposes a continuous entering gas and liquid flow, allowing an adjustment of the residence time of the liquid within the reactor [Rae88]. The residence time distribution of loop reactors is located between the ideal stirred tank reactor and the pipe reactor, providing a great adaptability for several different applications. A schematic sketch of a flow in a loop reactor is displayed in Figure 2-1 [Ble65].

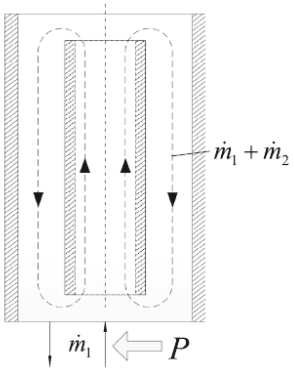

Figure 2-1: Schematic of a loop reactor with outgoing stream and power induced internal circulation [Ble71]

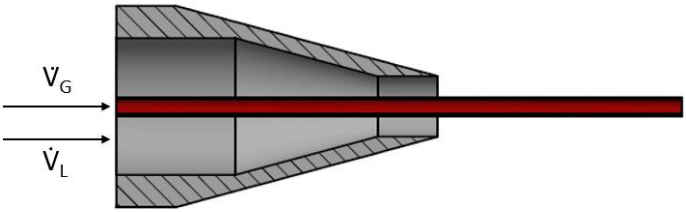

Figure 2-2: Nozzle head of a two-phase nozzle

A loop reactor driven by a nozzle is called jet loop reactor (JLR). The nozzle is either placed at the top or the bottom of the reactor and induces the necessary energy by momentum exchange at the free jet. Often two-phase nozzles are applied, using the momentum also for dispersing the gaseous phase, instantly generating high interfacial areas [Rae83]. A schematic sketch of a two-phase nozzle is displayed in *Figure 2-2*. The liquid flow V_L is pumped through the outer annular space and the gas flow V_G is being injected through the inner pipe. Usually, two-phase nozzles are based on the principle of injection or ejection. If a nozzle is operated as an injector, the gas is added under pressure and gets dispersed by the liquid jet. The gas accumulating in the head space of the reactor must be extracted and recompressed, before being reused. If a nozzle is carried out as an ejector, the momentum of the liquid flow induces suction, aspirating gas from a reservoir, for example the head volume. Therefore, the gas is reusable directly and without recompression [Wac85].

The nozzle can be placed either at the top or the bottom of the reactor, with both positions providing advantages and disadvantages. If the nozzle is placed at the top of the reactor, the gas is dispersed into the down streaming zone of the reactor and thus is forced to stream at least once through the down- and upstream zone of the reactor [Rae88]. However, this setup contains one major disadvantage. If the inserted momentum is too low, the gas cannot be transported through the draft tube and is rising within it, resulting in the collapse of the circulating flow. Also negative for

the loop stability is the presence of large bubbles with a higher rising velocity and residence time within the draft tube, resulting in coalescence and the collapse of the circulating flow [Loh90].

Caused by their simple design, the absence of moving parts and their compact design, jet loop reactors are already commonly used in chemical industry and biotechnology. Jet loop reactors usually stand out due to their high volumetric mass transfer performance, a convenient ratio of mass transfer area to energy dissipation density and clearly defined flow conditions. Additionally, jet loop reactors can be operated at elevated pressure and have a low demand of space, due to a large height to diameter (H/D) ratio [Rae88]. Important parameters for the characterization of gas-liquid jet loop reactors are the energy dissipation density P/V, the gas hold-up, the bubble size distribution and the circulation velocity of the gas-liquid mixture in the inner loop, expressed by the circulation number n. The important characteristics and the mentioned parameters used for this thesis are explained in detail in chapter 2.4 [Vog87].

2.3 Design of Jet Loop Reactors

This chapter is dealing with the design of jet loop reactors. Based on renowned literature, the most important design parameters and dimensions for a jet loop reactor with the injector nozzle placed within the headspace of the reactor are explained.

The volume of a reactor is based on the height, the diameter and a ratio of the height and the diameter must be chosen according to the used system. *Blenke* stated 1965 an ideal ration h/d = 5 for a single-phase system [Ble65], whereas *Bohner* is promoting a ration h/d = 7 for two-phase systems [Boh71]. As a result, the range of the ratio

$$5 \leq {}^{h}/_{d} \leq 7 \tag{2.13}$$

should be kept. In case the ratio is exceeded the amount of energy necessary to transport the gaseous phase downwards increases, resulting in a possible collapse of the circulating flow. If the ratio is smaller than five, the diameter of the draft tube must be greater, in order to use the entire reactor volume [Loh90].

The height of a reactor is the sum of the draft tub length, the distance between the draft tube and the deflector plate and the depth of coverage above the draft tube. For ideal operating conditions, all of quantities need to be adjusted to each other. The draft tube is used for guiding the flow in the desired way and taking care of a good momentum exchange between the driving jet and the two-phase mixture in the reactor. Therefore, the correct design of the draft tube length has an impact on the efficiency of the reactor. As the gas is getting pushed downwards and against the buoyancy forces of the bubbles, a ratio of draft tube length l_D and reactor diameter d_R of

$$4 \leq {}^{l_D}/_{d_R} \leq 5.5 \tag{2.14}$$

is recommended. [Loh90]

The distance of the deflection plate to the lower edge of the draft tube h_{DP} has an impact on the drag coefficient and the shape of the flow at the redirection. For preventing a constriction and congestion of the circulating flow during the redirection, the lateral surface below the draft tube must be at least equally sized as the cross-sectional area of the draft tube

$$\frac{\pi \cdot d_D^2}{4} = d_D \cdot \pi \cdot h_{DP} \rightarrow \frac{d_D}{4} = h_{DP} \qquad (2.15).$$

If the distance of the deflection plate to the lower edge of the draft tube is too low, the two-phase mixture is congested and the circulation collapses, while at much greater distances dead spaces can develop. [Loh90]

If the nozzle is placed in the head space of the reactor, the depth of coverage above the draft tube is important to prevent the circulation from collapsing. As new gas is being entrained and some remaining gas bubbles are aspirated back into the draft tube, the liquid level is oscillating heavily and in case the coverage is too small, the circulation might collapse. [Loh90]

Besides the design parameters above, the diameter and the shape of the draft tube have a large impact on the flowing conditions in the reactor. Usually, the draft tube edges are not shaped in any way, resulting in sharp edges, which tend to hinder an optimal flow. However, shaped draft tube edges with bulbs enhance the redirection and therefore minimize the drag coefficient [Ble71]. The diameter of the draft tube impacts the hydrodynamics of the reactor and the residence time characteristics. Therefore, it is used to fit the characteristics of a reactor to the needs. The upper limit for the draft tube diameter is given, when reaching equality of the cross-sectional area of the draft tube and the annulus space [Loh90].

In downstream jet loop reactors, the cross-sectional area of the draft tube is often smaller than the one in the annulus space, resulting in a higher velocity in the draft tube, which helps to float down the entrained gas. Commonly, the ratio

$$0.33 \leq {}^{d_D}/_{d_R} \leq 0.70 \tag{2.16}$$

is limiting the range of draft tube diameters [Loh90].

2.4 Characteristics of Jet Loop Reactors

In this chapter important quantities for the description and characterization of jet loop reactors will be explained.

2.4.1 Nozzle Outflow velocity

The nozzle outflow velocity is only depending on the liquid mass flow $\dot{m}_L$ pumped through the orifice and the available cross-sectional area A_N. Considering continuity (eq. 2.1) the nozzle outflow velocity w_N is defined by

$$w_N = \frac{\dot{V}_L}{A_N} = \frac{\dot{m}_L}{\rho_L \cdot A_N} \tag{2.17}$$

with A_N representing the available cross-sectional area of the orifice. The cross-sectional area of the orifice is reduced by the gassing tube. Thus, the available area results from

$$A_N = \frac{\pi}{4} \cdot (d_N^2 - d_{GT}^2) \tag{2.18}$$

with d_N representing the outer nozzle diameter and d_{GT} the diameter of the gassing tube.

The volume flow as well as the nozzle outflow velocity are important measures for the momentum transport into the gaseous phase and therefore for the dissipation of the gas in the liquid phase. [Wie11]

2.4.2 Superficial Velocity

The superficial liquid velocity w_L^0, respectively the superficial gas velocity w_G^0, is describing the velocity of a medium in a reactor without any sort of internals and in absence of other media. Therefore, the superficial velocity is only dependent on the reactor's dimensions and the volume flow of the medium. In case of a tubular reactor the reactor cross area is defined by

$$A_R = \frac{\pi}{4} d_R^2 \tag{2.19}$$

with d_R describing the diameter and A_R the cross area of the reactor. Taking only the superficial liquid velocity into account, comparing reactors becomes much easier. The superficial velocity

$$w_L^0 = \frac{\dot{V}_N}{A_R} = \frac{\dot{m}_N}{\rho_L \cdot A_R} \tag{2.20},$$

is considering the volume flow of the liquid $\dot{V}_N$ respectively the mass flow $\dot{m}_N$ and the corresponding density ρ_L. The superficial gas velocity $w_{g,0}$ is calculated like the superficial liquid velocity, using the corresponding fluid properties. [Kra12]

Since a loop reactor is containing an upstream- and a downstream zone, the superficial liquid velocity

$$w_L^0 = \frac{2\dot{m}_N}{\rho_L \cdot A_R} \tag{2.21}$$

in a loop reactor must be doubled [Wac86].

2.4.3 Energy Dissipation Density

The energy dissipation density P/V is a measure of the energy induced into the system. It is equal to the ratio of energy $\dot{E}_{kin}$ induced by the driving jet and the reactor volume V_R, yielding

$$\frac{P}{V} = \frac{\dot{E}_{kin}}{V_R} \tag{2.22}$$

The kinetic energy flow by the jet $\dot{E}_{kin}$ is calculated by the mass flow ṁ or volume flow $\dot{V}$ across the nozzle, the cross-section of the nozzle A_N and the density ρ of the used liquid, yielding for the liquid phase

$$\dot{E}_{kin} = \frac{\dot{m}_L}{2} \cdot w_N^2 = \frac{\rho_L}{2} \cdot \dot{V}_L \cdot w_N^2 = \frac{\rho_L}{2} \cdot w_N^3 \cdot A_N \tag{2.23}$$

By combining the equations 2.20 and 2.21 the expression

$$\frac{P}{V} = \frac{\rho_L \cdot w_N^3 \cdot A_N}{2 \cdot V_R} \tag{2.24}$$

is derived, often used to calculate the energy dissipation [Loh90].

In case the reactor is operated with active gassing, an energy flux is induced by the gas flow. The kinetic energy flow of the gas is calculated as the kinetic energy of the liquid, considering the properties of the gas and the dimensions of the gassing device. The equation for calculating the energy dissipation density is extended by the kinetic energy resulting from the gassing. Extending equation 2.22 by the kinetic energy flux of the gas yields

$$\frac{P}{V} = \frac{\rho_L \cdot w_N^3 \cdot A_N}{2 \cdot V_R} + \frac{\rho_G \cdot w_{GT}^3 \cdot A_{GT}}{2 \cdot V_R} \tag{2.25}$$

As the adjusted gas flux is very small compared to the liquid flow, the energy dissipation caused by the gas is neglected. [Loh90]

The energy dissipation density is important for the description of the flow conditions in reactors and has significant influences on mixing processes, mass transfer and phase interfaces. However, the lack of precise data leads towards a simplification, resulting in the assumption of a locally equal distribution of the energy dissipation density within the reactor volume. This simplification causes discrepancies in between theoretical and

experimental work, showing the need and challenge of the precise estimation of the energy dissipation density in a system. [Wie11]

2.4.4 Gas Hold-Up

The gas hold-up is an important operating parameter not only for loop reactors, but any multiphase system. It provides information on the phase fractions and is crucial for the mass transfer of the gaseous and liquid phase. The gas hold-up is dependent on the gas load and the used gas-liquid systems. The gas hold-up is defined as the fraction of the gaseous phase of the total volume and is calculated by

$$\epsilon_g = \frac{V_g}{V_g + V_L} \tag{2.26}$$

with ϵ_g representing the gas hold-up, V_g the gas volume and V_L the liquid volume. As the volume of a loop reactor

$$V_x = \frac{\pi}{4} \cdot d_R^2 \cdot h_x \tag{2.27}$$

is only dependent on the base area and the height h_x, equation 2.24 can be rewritten and simplified to

$$\epsilon_G = \frac{h - h_0}{h} = \frac{\Delta h}{h} \tag{2.28}$$

Therefore, the gas hold-up can be calculated by knowing the initial fluid level without gassing h_0 and the fluid level under operating conditions. [Kra12]

Using this universal approach for estimating the gas hold-up, it is important to subtract the volume of the draft tube as well in order to get correct values. Otherwise the gas hold-up would be underestimated.

The gas hold-up strongly depends on the gas-liquid system used. Therefore, correlations have been determined in the past to predict the gas holdup. Well known is the correlation of Akita and Yoshida stated in 1973,

which can be applied for a broad range of gas-liquid systems and is defined by

$$\frac{\epsilon_g}{(1-\epsilon_g)^4} = 0.2(Bo)^{1/8}(Ga)^{1/12}(Fr) \qquad (2.29),$$

depending on the Bond, Galileo and Froude number [Aki73]. Another correlation, stated by Jamshidi in 2001 and fitted for downstream jet loop reactors, estimates the gas hold-up with a relative error of ±20%. The correlation allows calculating the gas hold-up

$$\epsilon_g = 1.1072 \cdot 10^{-4}(Re)^{1.095}(Fr)^{0.885}\left(\frac{d_D}{d_R}\right)^{0.025}\left(\frac{1.4L_D}{1+2H_N}\right)^{0.9} \qquad (2.30)$$

by correlating the Reynolds- and Froude number as well as the reactor dimensions and the distance of the nozzle to the draft tube H_N [Jam01a].

2.4.5 Bubble Behavior

In a gas-liquid jet loop reactor, knowledge about the bubble behavior is crucial, since the bubble behavior strongly affects the flow regime, the gas hold-up and the mass transfer.

In contrast to solid particles, the interfaces of bubbles are usually in motion. As a result of the surrounding liquid flow, the inner volume of the bubble starts to circulate, shown *Figure 2-3*. Furthermore, the geometrical shape of the bubble is changing, depending on the bubbles size. For small diameters, the bubble is spherical. If a certain diameter, depending on the physical properties of the gas and liquids used, is exceeded, the bubble starts to deform. As a result, the bubble will first form into an ellipsoid and, with increasing size, the shape is unsettled. The typically occurring shapes are shown in *Figure 2-3*. After reaching a critical size, the bubble becomes instable and is breaking up into smaller bubbles [Kra12].

After the generation of the bubbles, the acting forces result in an acceleration of each bubble until an equilibrated state is reached. The forces acting on a bubble are in general the weight force F_g

$$F_g = \frac{\pi}{6} \cdot d_B^3 \cdot \rho_G \cdot g \qquad (2.31),$$

the buoyancy force F_b

$$F_b = \frac{\pi}{6} \cdot d_B^3 \cdot \rho_L \cdot g \qquad (2.32)$$

and the drag force F_d

$$F_d = \frac{\pi}{4} \cdot d_B^2 \cdot \rho_L \cdot \zeta \cdot \frac{w_B^2}{2} \qquad (2.33).$$

with d_b describing the bubble diameter, ρ_G the density of the gas, ρ_L the density of the liquid, g the acceleration of gravity and ζ the drag coefficient. Setting up a force equilibrium of those acting forces yields

$$w_B = \sqrt{\frac{4}{3} \cdot \frac{|\rho_L - \rho_G|}{\rho_L} \cdot \frac{g \cdot d_B}{\zeta}} \qquad (2.34),$$

used for calculating the relative bubble velocity. [Kra12]

As a result of the changeable interface, some additional effects need to be considered, if the movement of bubbles is to be determined. Especially the definition of a generally valid drag coefficient is difficult, due to the complex interactions of the bubble shape and flow conditions, which depend on the compressibility and differences of density. With increasing diameter, the drag coefficient of a bubble first falls linearly, until a critical Reynolds number is reached. Then it rises again, until reaching a stable maximum, see *Figure 2-3*. [Vdi13b]

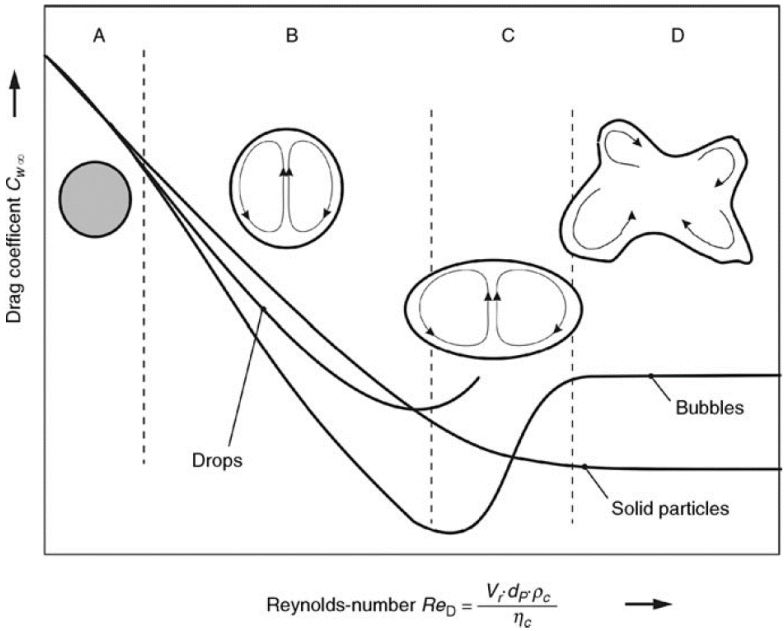

Figure 2-3: Schematic of the drag coefficient dependent on the Reynolds number for solids, drops and bubbles [VDI13b]

For characterizing the movement behavior, determining bubble shape, often the generalized graphical correlation proposed by *Grace* is used. The approach is correlating the Eötvös, Morton and Reynolds number and covers a broad range of fluid properties and bubble volumes. The correlation as displayed in *Figure 2-4* may be used for the determination of shape regimes and terminal velocities. [Cli78]

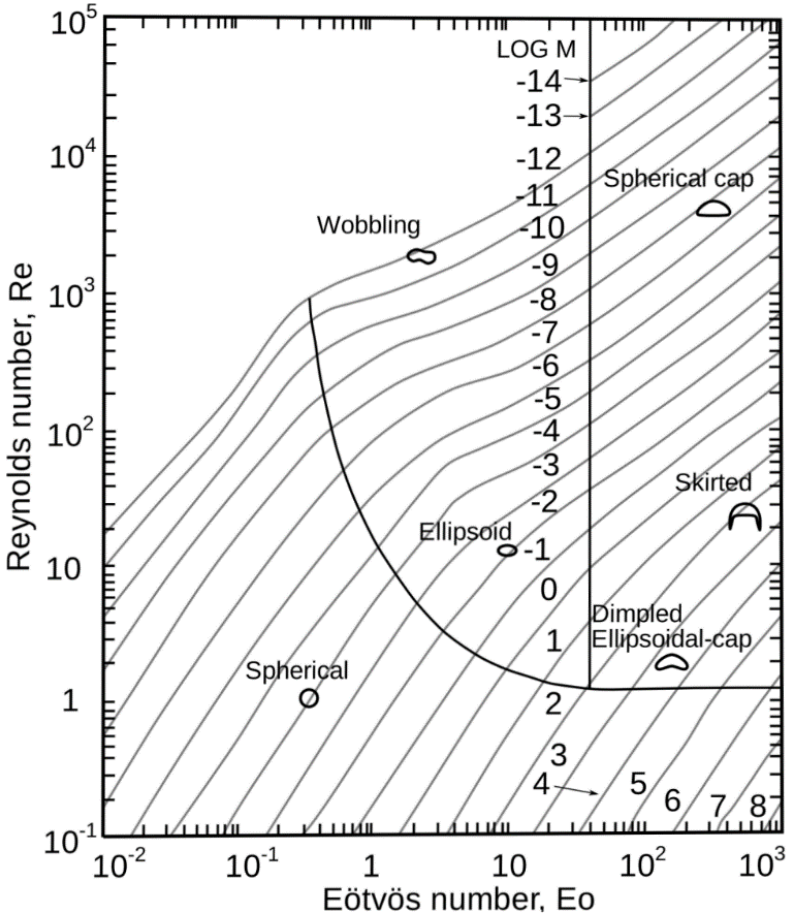

Figure 2-4: Grace diagram showing the shape regimes for bubbles and drops in unhindered gravitational motion in liquids [Gra76]

Within common technical applications, bubbles usually are present as bubble swarms with several bubbles, influencing each other. The rising velocity of bubbles in a swarm and in a stationary flow is the result of equilibrium of the occurring drag forces and the buoyancy forces without

the weight forces. This equilibrium is set up for the largest stable bubble diameter

$$d_E = 3 \cdot \sqrt{\frac{\sigma}{\Delta\rho \cdot g}} \qquad (2.35),$$

which is depending on the density ρ_L, the surface tension σ, the acceleration of gravitation g and the density of the gaseous phase ρ_G. With d_E known, the force equilibrium of a bubble rising in a swarm can be set up. Considering the void fraction of the dispersed gaseous phase φ_g yields

$$\zeta_E \frac{d_E^2 \cdot \pi \cdot w_s^2 \rho_L}{8} = \frac{\pi \cdot \Delta\rho(1-\varphi_g) \cdot g}{6} \qquad (2.36),$$

with ζ_E representing the drag coefficient of the largest stable bubble and the swarm velocity w_s

$$w_s = \frac{w_G^0}{\varphi_g} \qquad (2.37),$$

taking continuity and the superficial gas velocity into account. Inserting (eq. 2.34) into (eq. 2.33) allows calculating the drag coefficient as well as the void fraction by rearranging and solving for the wished quantity. Since the rising velocity in the bubble swarm is lower than the rising velocity of a single stable bubble ($\varphi_v > 0$), the rising of a single bubble cannot be expressed by the superficial velocity and the void fraction. [Mer77]

For evaluating bubble swarms, the bubble size distribution is an important quantity. There are several methods for measuring the bubble size distribution, like laser optical or fiber optical systems. Fiber optical systems are based on changing reflections while piercing a bubble. The recorded data is geometrically evaluated. As not all bubbles have an ideal spherical shape, an equivalent diameter is important for evaluation. A commonly used equivalent diameter is the mean Sauter diameter

$$d_{sa} = \frac{6 \cdot V_{tot}}{S_{tot}} \quad (2.38),$$

considering the total surface S_{tot} and the total volume V_{tot} of all measured bubbles. Knowing the mean Sauter diameter and the gas hold-up ε_G of a gas/liquid system allows the calculation of the specific interface

$$a = \frac{6 \cdot \epsilon_G}{d_{sa}} \quad (2.39),$$

which is an important quantity while observing the mass transfer. [Mer86]

2.5 Mass transport

If two or more phases are brought into contact, they will strive to reach an equilibrium state. The driving forces of this phenomenon are concentration-, pressure and temperature gradients. Within this chapter the driving force of interest are the concentration gradients $\Delta c_{i,j}$, resulting in the transport of molecules from phase *i* across the interfacial area into phase *j*. The occurring mass transport takes place without an outer constraint and is called molecular mass transport or diffusion. In case the contacted phases are in motion, the mass transport is added by a convective part in the direction of flow, which is usually much greater than the diffusion. [Bae16]

2.5.1 Molecular mass transport

For representation of the molecular mass transport usually the mass flux density $\dot{m}$ or the mole flux density $\dot{n}$ are used. Diffusion or molecular mass transport occur in mixtures of at least two homogeneous components with different concentrations c_i and c_j. Based on the random movement, the Brownian motion, of the molecules, a transient occurs until the concentration gradients Δc_i and Δc_j are compensated. This procedure results in a mole flux $\dot{N}_i$ in direction of declining concentration and a flux of $\dot{N}_j$ in the opposite direction, as a result of continuity. In case both fluxes have

the same value, the process is named equimolar diffusion. Usually the diffusion is not equimolar, but bilateral as a result of sinks or sources due to chemical reactions. A limiting case of the non-equimolar diffusion is the unidirectional diffusion. [Kra12]

The equimolar diffusion is present if two equally sized mole fluxes in opposing directions exist. The equimolar diffusion is occurring in either solid or stationary fluids as well as in laminar flows and can be determined under consideration of Fick's law of diffusion at constant density. The calculation of the mole flux densities is carried out by

$$\dot{n}_i = -D_{i,j} \cdot \frac{dc_i}{dx} \tag{2.40}$$

for one direction and

$$\dot{n}_j = -D_{j,i} \cdot \frac{dc_j}{dx} \tag{2.41}$$

in the opposite direction. D represents the diffusion coefficient and its indices i,j or j,i indicating the direction of the fluxes. The relationship

$$\dot{n}_i = -\dot{n}_j \tag{2.42}$$

is connecting the mole flux densities. This relationship shows that for ideal gases no volume change is occurring. Therefore, this phenomenon is called constant volume diffusion. Instead of mole flux densities and concentrations, it is possible to calculate with mass flux densities

$$\dot{m}_i = \dot{n}_i \cdot \overline{M} \tag{2.43}$$

and partial densities

$$\rho_i = \overline{M} \cdot c_i \tag{2.44},$$

which are both based on the mean molar mass M. [Kra12]

A limiting case of molecular diffusion is the unidirectional diffusion, where only one substance is defusing, without a mole flux of the other

component defusing backwards. This happens for example at semipermeable membranes or if phase *i* is already saturated with phase *j*. Another typical example for unidirectional diffusion is the diffusion of a liquid in an open cylindrical vessel into the surrounding gas. If the partial pressure of the liquid at the surface is greater than in the gas above the liquid, it starts to evaporate. On the other side the gas molecules are not able to pass the interface. For continuity reasons a displacement flow (Stefan-flow) causes a circulation of the gaseous phase. This effect is also known as Stefan-diffusion. [Bae16]

2.5.2 Convective mass transport

Convective mass transport occurs, if mass is not only transported by the molecular exchange, but also by the macroscopic motions of the fluid. The convective mass transport depends on the type of fluid flow and the substance properties. Convection can be forced, as a result of pumping, or free, as a result of density or temperature differences. For calculating the mass transport across the interfaces of two or more fluids the mass transfer coefficient β is introduced. The mass transfer coefficient is a theoretical quantity and has no direct physical meaning, since both transport mechanisms are undifferentiable combined. Generally, the equation for the mole flux Ṅ across interfaces is

$$\dot{N}_i = \beta \cdot A \cdot (c_i^* - c_i^\infty) = \beta \cdot A \cdot \Delta c_i \tag{2.45}$$

or, if divided by the interfacial area,

$$\dot{n}_i = \beta \cdot (c_i^* - c_i^\infty) = \beta \cdot \Delta c_i \tag{2.46}$$

with A as the interfacial area, c_i^* as the concentration right at the interface and c_i^∞ the concentration far away from the interface in the continuous phase. For a better illustration the mass transport from a bubble into a surrounding liquid is illustrated in *Figure 2-5*.

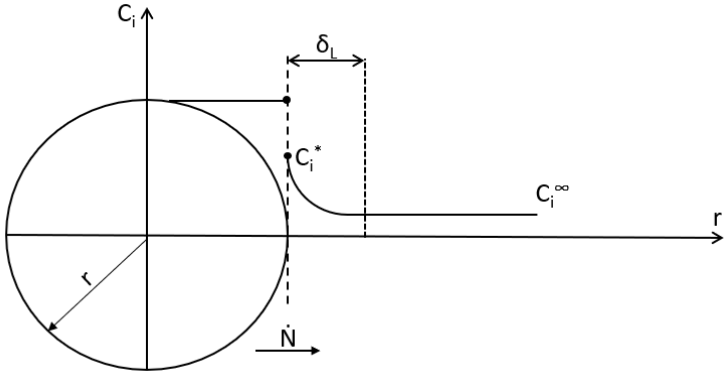

Figure 2-5: Stationary mass transport at a gas bubble in the surrounding phase according to [Bra71]

The mole flux across the interface stays constant, until the equilibrium is reached, and the concentration gradient is consumed. As mentioned before, the mole flux usually is going in both directions. Therefore, the mole flux between the gaseous phase and the liquid phase is either

$$\dot{n}_i = \beta_G \cdot \left(c_{i,G}^{\infty} - c_{i,G}^{*}\right) \tag{2.47}$$

or the other way around

$$\dot{n}_i = \beta_L \cdot \left(c_{i,L}^{*} - c_{i,L}^{\infty}\right) \tag{2.48}.$$

The derived equations 2.45 and 2.48 are the theoretical background of the mass transport, but their use is limited, since the concentration c* is hard to measure. Therefore, mass transport must be evaluated, using different mass transport theories. The most commonly known ones are the penetration theory, the surface renewal theory and the two-film theory, which will be explained in detail in the following chapter. Most theories have in common, that they are providing the volume specific mass transfer coefficient $\beta_L a$, which is a product of the mass transfer coefficient and the specific surface, displayed in equation 2.35 in the previous chapter [Bae16].

2.5.3 Two-film theory

The two-film theory is describing the mass transport from a gaseous phase into a liquid phase. Since the mass transport at the interface is much faster than the transport within each phase, the mass transport resistance at the interface is neglected and an equilibrated state at the interface is assumed. The mass transport is only caused by diffusion. A differential equation

$$\dot{V}_L \cdot \frac{dc_L}{dV_R} = \beta_L a \cdot (\rho_L^* - \rho_L) \tag{2.49}$$

for the mass transport can be derived. It contains the liquid volume flow $\dot{V}_L$, the volume of the reactor V_R, the volume specific mass transfer $\beta_L a$, the saturation density of the gas in the liquid ρ_L^* and the actual species density of the gas ρ_L. Integrating (eq. 2.49) over the volume and using the entering concentration $c_{G,i}$ and the outgoing concentration $c_{G,o}$ as boundaries, an equation for $\beta_L a$ can be derived

$$\beta_L a = ln\left(\frac{c_G^* - c_{G,o}}{c_G^* - c_{G,i}}\right) \cdot \frac{\dot{V}_L}{V_R} \tag{2.50},$$

describing the mass transport from the gaseous into the liquid phase. [Bae16]

According to Henry's law, the concentration and the partial pressure follow a linear trend, allowing to calculate the saturation concentration of the gaseous phase in the liquid phase by

$$c_G^* = H_G(T) \cdot p_G \tag{2.51},$$

using the Henry constant of the gas H_G and the partial pressure of the gas p_G. [Mer86]

2.5.4 Mass transport at Bubbles

The mass transport at rising bubbles is mainly determined by the flow conditions in their direct vicinity. For the approximation of the mass transport at single bubbles, several empirical correlations have been developed. In case the bubble size d_B and the diffusion coefficient D are known, the mass transport coefficient can be determined, using the Sherwood number (eq. 2.10). In literature many correlations for single bubbles exist. They are usually a function of the Reynolds and Schmidt number

$$Sh = 2 + C \cdot Re^a \cdot Sc^b \qquad (2.52),$$

allowing the calculation of a Sherwood number for different bubble shapes and flowing conditions. The known correlations can be divided into two groups., correlations for bubbles with a stable shape and bubbles with a varying shape. [Gla77]

The empirical correlation for bubbles with a stable shape under sidle flow conditions $Re \rightarrow 0$,

$$Sh = 2 + \frac{0.651(ReSc)^{1.71}}{1 + (ReSc)^{1.22}} \qquad (2.53),$$

was stated by *Schmidt-Traub* in 1970. If $ReSc \rightarrow 0$, the Sherwood number is converging towards two $Sh \rightarrow 2$. If $ReSc \rightarrow \infty$, the equation 2.52 is resulting in the limiting law for spherical bubbles,

$$Sh = 0.65(ReSc)^{0.5} \qquad (2.54),$$

stated by *Levic* in 1962. As the Reynolds number is converging towards zero $Re \rightarrow 0$, the Schmidt number must run towards infinity $Sc \rightarrow \infty$ for $ReSc \rightarrow \infty$, resulting in a rather thin boundary layer compared to the bubble diameter. [Gla77]

For stable bubbles and high Reynolds numbers $Re \rightarrow \infty$, the empirical correlation

$$Sh = 2 + \frac{0.232(ReSc)^{1.72}}{1 + 0.205(ReSc)^{1.22}} \tag{2.55}$$

is used. In case the product of the Reynolds- and Schmidt number is running towards infinity $ReSc \rightarrow \infty$, the limiting law of *Boussinesq*

$$Sh = 1.13(ReSc)^{0.5} \tag{2.56}$$

can be derived. [Gla77]

Shape variable bubbles usually have a greater surface than shape stable bubbles. The determination of the mass transport coefficient at shape variable bubbles is considering a volume equal diameter like the mean Sauter diameter (see equation 2.35). As a result of different studies, an empirical correlation

$$Sh = 2 + 1.5 \cdot 10^{-4} Re^{0.89} Sc^{0.7} \tag{2.57}$$

representing shape variable bubbles was derived by *Gläser*. [Gla77]

In *Figure 2-6* the experimentally determined mean Sherwood numbers are resolved against the product of the Reynolds- and Schmidt number.

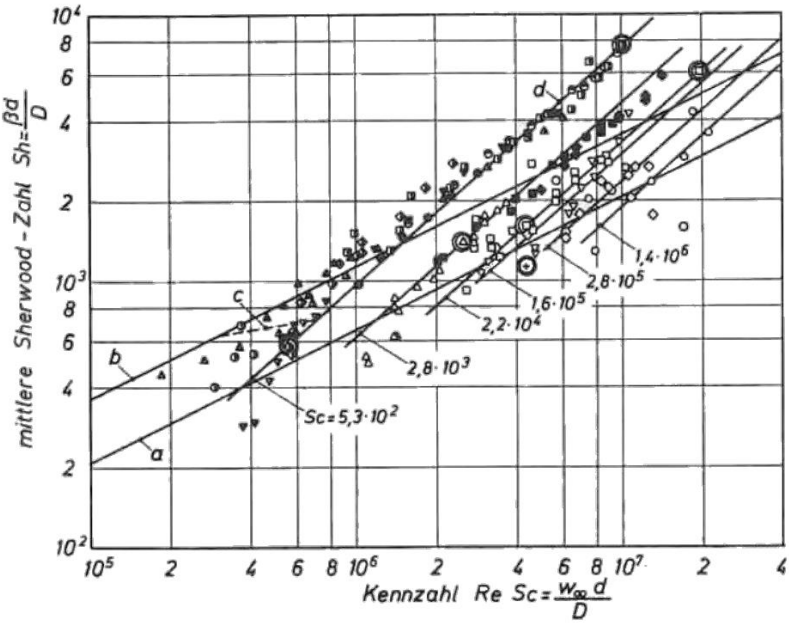

Figure 2-6: Mean Sherwood number in dependency of (ReSc) for different values of Sc. Displayed are the upper and lower boundaries for stable, spherical bubbles (a) and (b), the transition area of stable bubbles and variable bubbles (c) and variable bubbles (d) according to [Gla77]

2.5.5 Mass transfer in Jet Loop Reactors

The mass transfer in jet loop reactors is not depending on a single bubble, but rather on the complex mechanisms acting due to the movement of bubble swarms. Therefore, empirical correlations for determining the mass transfer have been developed in the past.

A general approach applicable for bubble columns is given by *Zehner & Kraume*. The approach is, that the volumetric mass transfer coefficient and the gas rate

$$\beta_L a \propto \dot{V_g^n} \tag{2.58}.$$

are proportional to each other [Zeh05].

This proportionality is used by *Prasad et al*., who state an approach for the calculation of the volumetric mass transfer coefficient

$$\beta_L a = 0.02 \cdot (w_g^0)^{0.6} \tag{2.59},$$

adding a constant for a better approximation [War16].

A second approach is using the proportionality of the volumetric mass transfer coefficient and the gas. Proposed by *Farizoglu et al*., an addition to the first approach is made by adding the energy dissipation density to the term

$$\beta_L a = 23.38 \cdot \left(\frac{P}{V_R}\right)^{0,17} \cdot \dot{V_G}^{0.8} \tag{2.60}$$

and adjusting the constant and exponent regarding the gas rate [War16].

As a final step *Jamshidi et al*. give a dimensionless expression, based on the already introduced Sherwood number (eq. 2.10). Like the approaches stated by *Gläser* for single bubbles, the correlation for a jet loop reactor is considering the Schmidt- and Reynolds number and is extended by the Morton- and Froude number and a relation of the draft tube length l_D combined with the nozzle length l_N. Those assumptions result in

$$Sh_{ind} = 1.76 \cdot Sc^{0.5} \cdot Re_N^{0.99} \cdot Fr^{0.5} \cdot Mo^{-0.06} \cdot \frac{0.15 + 1.05 l_D}{l_D + l_N} \qquad (2.63),$$

acting as a dimensionless correlation for predicting the mass transfer in jet loop reactors [Jam01b].

A common way of comparing different jet loop reactor systems, is by plotting the volume specific mass transfer coefficient $\beta_L a$ with the energy dissipation density as displayed in *Figure 2-7*.

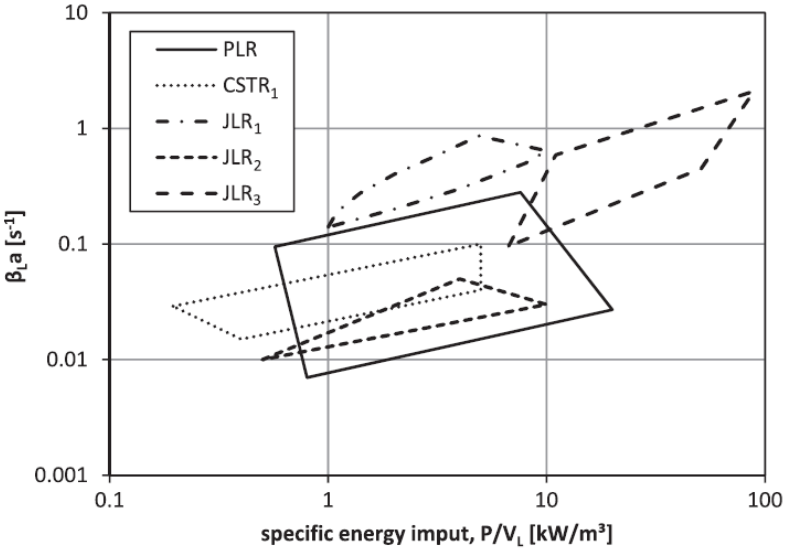

Figure 2-7: Plot of volume specific mass transfer coefficient $\beta_L a$ against the specific energy input P/V for different reactor types [War16]

3 Methodology and Materials

This chapter is describing the dimensioning of the reactor, the experimental setup, the used measurement techniques and devices and the experimental procedure needed for this thesis. The reactor characteristics are evaluated by measuring the oxygen concentration, using flow-through cells, a fiber optical probe for the determination of the bubble sizes and rising velocities and a high-speed camera for the verification of the measured bubble parameters.

3.1 Reactor Design

The designed reactor is a downstream jet loop reactor as described prior. The reactor is designed for a total liquid volume of $V_R = 20\ L$ and is driven by a top-down nozzle, resulting in a downstream jet loop reactor. According to the work of *Lohrengel*, a ratio of $h/d = 5$ is chosen. Combining all information, allows the calculation of the necessary diameter by

$$d_R = \sqrt[3]{\frac{4 \cdot V_R}{5 \cdot \pi}} = 172mm = 0.172m \tag{3.1}$$

and the resulting height for containing a volume of *20 L* by

$$h_R = 5 \cdot d_R = 860mm = 0.86 \tag{3.2}.$$

As the reactor must have a head space for the gaseous phase, the total length of the reactor is *1000 mm* or *1 m*.

The dimensions of the experimentally used reactor are shown schematically in *Figure 3-1* and are explained in *Table 3-1*.

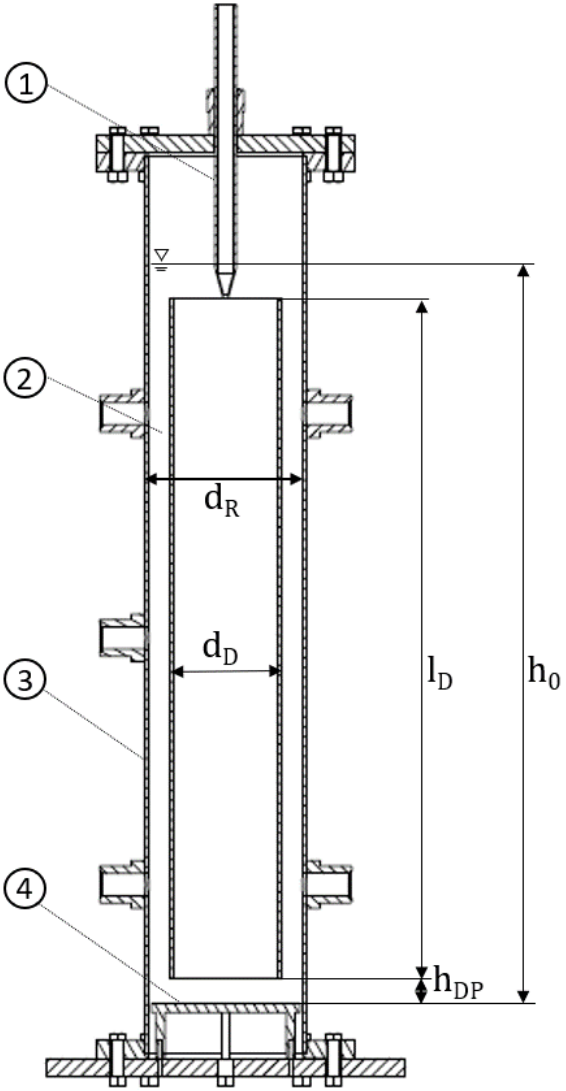

Figure 3-1: Schematic of the reactor including the important dimensions and important components (1) nozzle, (2) draft tube, (3) reactor and (4) deflection plate

Table 3-1: Reactor dimensions used for the experimental work

Symbol	*Meaning*	*Value /mm*
$\mathbf{l_D}$	draft tube length	758
$\mathbf{h_0}$	starting liquid level	830
$\mathbf{h_{DP}}$	distance draft tube – deflection plate	29
$\mathbf{d_{DP}}$	diameter deflection plate	165
$\mathbf{d_R}$	inner diameter reactor	172
$\mathbf{d_D}$	inner diameter draft tube	115

By knowing the diameter and the height of the reactor, the length of the draft tube can be determined. In literature, a range as shown in eq. (2.41) is advised. *Blenke* proposed an ideal length of the draft tube of $l_D/d_R = 4.4$. Considering all given information and the already calculated proportions of the reactor, the length of the draft tube is determined to be 758 mm, which is equal to a ratio of $l_D/d_R = 4.4$.

In the next step the diameter of the draft tube is calculated. The reactor is designed under the proposition that the equality of the cross-sectional areas is fulfilled. This means, that the annulus area of the rising part has the same size, than the area of the draft tube in the middle of the reactor. This condition results in

$$A_{AS} = \frac{\pi}{4} \cdot \left(d_R^2 - d_{o,D}^2\right) = \frac{\pi}{4} \cdot d_D^2 = A_D \qquad (3.3).$$

As a result of this condition, a draft tube with an inner diameter d_D = 115 mm and an outer diameter $d_{o,D}$ = 125 mm is chosen, resulting in an annulus space A_{AS} = 10963 mm² and an area of the draft tube A_D = 10386 mm², meeting the condition of equal cross-sectional areas sufficiently.

Based on the same proposition, the distance of the draft tube and the deflection plate h_{DP} is calculated. The assumption that the lateral surface below the draft tube is equal to the cross-sectional area of the draft tube results in

$$A_M = \pi \cdot d_D \cdot h_{DP} = \frac{\pi}{4} \cdot d_D^2 = A_D \tag{3.4}$$

$$h_{DP} = \frac{1}{4} \cdot d_D = 28{,}75mm \cong 29mm \tag{3.5},$$

allowing the exact calculation of the distance between the draft tube and the deflection plate.

For the prevention of air entrainment into the pump, the deflection plate is mounted 60 mm above the actual bottom of the reactor. As only the liquid level above the deflection plate is counted as the active volume used, the total liquid level is at 920 mm for keeping the h/d ration and the desired volume of 20 L. Experiments conducted in the bachelor thesis of *D. Schnute* [Sch19] show that a liquid level of 880 mm provides more stable operating points, resulting in a total volume of about 19 L. This corrected liquid level also changes the *h/d* ratio to *h/d = 4.8*. Due to the greater ratio of draft tube to reactor diameter, this is a reasonable change of the design and setup according to the literature and *Lohrengels* suggestions.

Knowing all dimensions of the reactor, allows designing the two-phase nozzle and the diameter of the deflection plate. For establishing the circulating flow in the reactor, usually an energy input greater than $P/V = 1 kWm^{-3}$ is necessary. Based on the minimum energy input needed and the nozzle dimensions in the master thesis of *C. Busch* [Bus17], the dimensions of the nozzle are calculated, resulting in a nozzle with an opening angle $\varphi = 15°$ for an optimal flow and the dimensions shown in *Figure 2-1*. The distance of the gassing tube to the end of the nozzle results from the available experimental data of *Lohrengel* and is calculated by

$$e = C \cdot \frac{d_N - d_{GT}}{C_m} \tag{3.6},$$

referring to the laws of free jets and using the coefficients $C = 1.6$ and $m = 0.3$, which are based on the experimental work [Loh90].

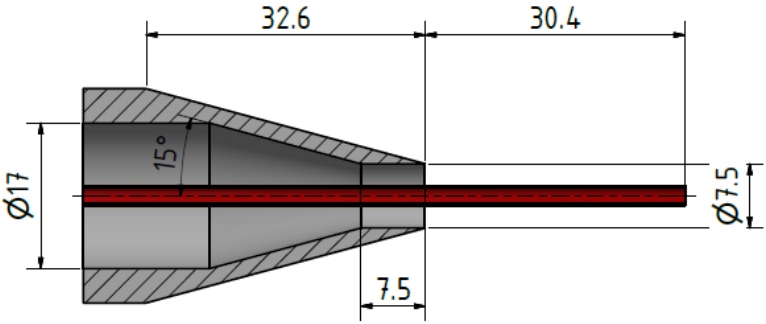

Figure 3-2: Technical drawing of the used two-phase nozzle

As a result of the dimensions of the nozzle, the reactor volume and the energy input, the occurring volume flows and velocities at the nozzle outlet are calculated by rearranging equation (2.23), resulting in the values listed in *Table 3-1*.

Table 3-2: Resulting velocities w_N and volume fluxes V_L at the nozzle

P/V /kWm^{-3}	1	1.5	2	2.5	3	3.5	4
w_N /ms^{-1}	10	11.5	12.6	13.6	14.5	15.2	15.9
V_L /m^3h^{-1}	1.4	1.63	1.8	1.94	2.07	2.17	2.27

The diameters of the deflection plate at the bottom of the reactor must be large enough, to prevent air getting entrained into the pump. If the diameter of the deflection plate is too close to the diameter of the reactor, the

velocity in the annulus space is higher than the rising velocity of the bubbles and air is getting sucked into the system as well. The chosen diameter of d_P = 165 mm results in a velocity range of 0.2 to 0.3 ms^{-1}, depending on the actual circulating volume flow, and is low enough to prevent bubbles from getting entrained.

A part of this thesis is the comparison of different draft tube shapes. As a benchmark system, a cylindrical draft tube with sharp edges made of Poly-(methyl)-methacrylate (PMMA), also known as acrylic glass, with the calculated inner diameter of d_D = 115 mm was used. As an alternative to the traditional setup, a 3D-printed draft tube with a drop shaped widening at both edges was designed, based on the results of the work of *Blenke* [Ble71]. The shape and the dimensions of the used draft tubes are displayed in *Figure 3-3* beneath.

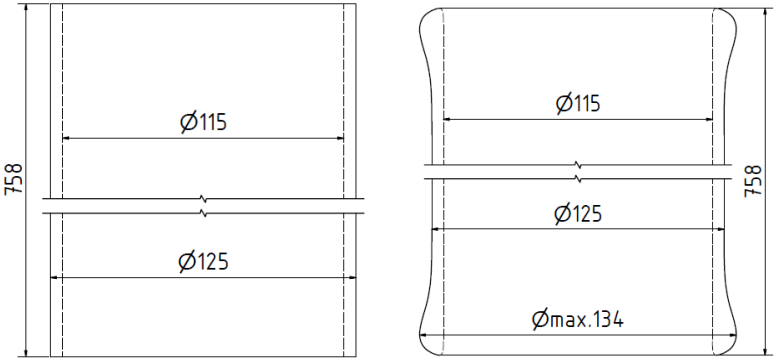

Figure 3-3: Technical drawings of the two different draft tube designs cylindrical pipe and flow optimized

For the experimental work within this thesis two different draft tubes are investigated and compared. Next to the cylindrical draft tube, a second draft tube is flow optimize. It is made of acrylic glass, combined with the 3D-printed widenings using a resin and the SLA printing method.

3.2 Measurement Techniques

In this chapter the flow-through cells of PreSens Sensing and the fiber optical probe of A2 Photonics, which are used for this thesis, are explained in detail.

3.2.1 PreSens Oxy1-SMA-Pst3 FTM

Measuring the oxygen concentration precisely, is a crucial element for the determination of the volumetric mass transfer coefficient $\beta_L a$ in a gas-liquid system. As this jet loop reactor is used as a separate gassing element within a larger process, online measuring of the oxygen concentration is important. The used system of the PreSens Precision Sensing GmbH contains three main parts: the flow through cell, the Pst3- oxygen probe and the OXY1-SMA processing unit. The entire system is shown in *Figure 3-4* beneath.

Figure 3-4: Measuring system FTM-Pst3 and processing unit OXY1-SMA

The flow through cell itself is a standardized Swagelok T-fitting with an inner diameter of 1/8" and is made of stainless steel. The processing unit OXY1-SMA is attached directly to a PC by a USB connector and to a Pst-3

oxygen probe via an optical SMA connector. The Pst3-oxygen probe is placed tightly screwed into the flow through cell and is placed in such manner, that the sensing spot at the tip of the probe is located within the observed fluid. The important technical information as measuring range, lower detection limit, resolution, precision, response time and temperature range of the Pst-3 probe are listed in *Table 3-3* below.

Table 3-3: Technical data of the Pst3-oxygen probe of Presens Precision Sensing [PRE19]

Specification	***Gaseous O_2***	***Dissolved O_2***
Measuring Range	0 -100 %	0 – 45 mgL^{-1}
Lower Detection Limit	0.03 % O_2	15 ppb
Resolution	± 0,01 % O_2 (0,21 %) ± 0,1 % O_2 (20,9 %)	± 0,004 mgL^{-1} (0,091 mgL^{-1}) ± 0,04 mgL^{-1} (9,1 mgL^{-1})
Precision	0,4 % O_2 (20,9 %) ± 0,05 % O_2 (0,2 %)	-
Response Time (t_{90})	< 6s	< 40s
Temperature Range	0°C – 50°C	

The measuring principle of chemical-optic probes like the used Pst3-probe is based on fluorescing indicator pigments, sensitive regarding the desired analyte. The pigments are embedded in a polymer matrix, which is placed as a sensor spot in the observed fluid. A LED is stimulating the pigments, which emit a fluorescence glow. If an oxygen molecule is hitting the sensor spot, the excess energy is transferred to the molecule, quenching or decreasing the fluorescent signal. The degree of quenching is correlating to the partial pressure of oxygen in the matrix, which is equilibrated with the oxygen within the sample. For a better understanding, a schematic of the described measuring principle is displayed below in *Figure 3-5*. [PRE19]

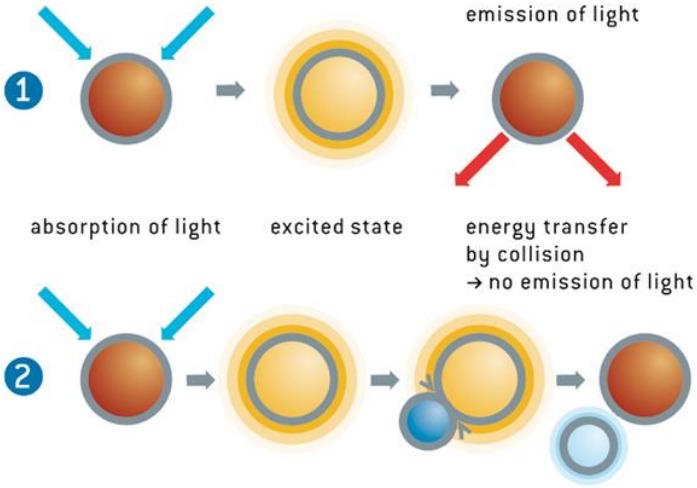

Figure 3-5: Measuring principle of chemical-optical oxygen measurements [PRE19]

3.2.2 A2 Photonics fiber optical probe

Knowledge about the bubble sizes in a multiphase gas-liquid reactor is an important quantity for calculating the specific area and therefore the mass transfer coefficient β_L. A system for measuring the bubble sizes without the need of an optical access to the reactor is the A2-Phonotnics fiber optical probe, which is used within this thesis. The used system consists of two parts, the control unit and the fiber optical probe, which is connected to the control unit by a fiber optical cable. The fiber optical probe has a sharply grinded tip with a diameter of about 125 µm. The dimensions of the probe and the stainless steel supporting structure are given in the technical sketch *Figure 3-6*.

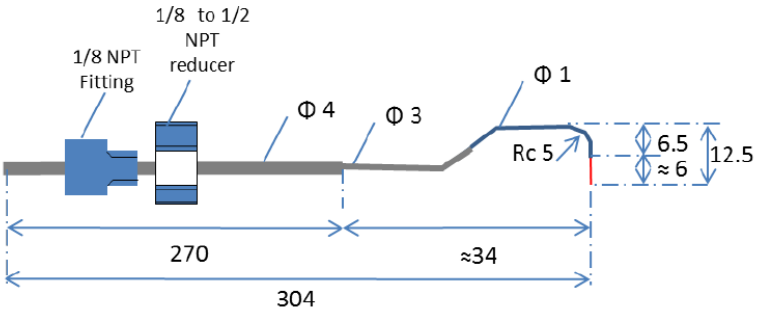

Figure 3-6: Technical drawing of the A2-Photonics fiber optical probe, dimensions are given in mm [Zua13]

The working principle of the system is based on the change of reflection, caused by the changing phases, while piercing a bubble. The control unit is emitting an adjustable laser light in a range of 0 – 20 mA which is reaching the tip of the probe. The probe is placed within the observed flow, facing in the opposite direction of the bubble trajectory. The measuring principle is explained at the example of a typical observed signal, given in *Figure 3-7*.

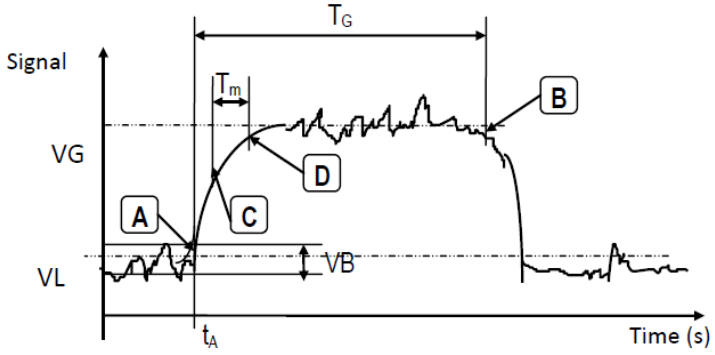

Figure 3-7: Typical signal signature of a bubble piercing the tip of the probe [ZUA13]

When the light signal reaches the tip, it is getting reflected based on the phase the probe is currently surrounded by. The reflected signal, reentering the control unit, is converted into a -10V - +10V signal and is at the level of *VL,* while being in the liquid phase and *VG* in the gaseous phase. Marked with (A) is the moment the tip begins to pierce a bubble and with (B) the end of the detected bubble. The residence time of the probe in the bubble is named T_G and is giving the information about the size of the bubble, based on the duration the probe spends within the bubble. The interval between the spots (C) and (D) is the time of the transition from the liquid into the gaseous phase, called rising time T_m and is used to calculate the absolute velocity of the bubble. Based on the acquired data, the velocity and the size can be directly derived. The advantage of this technique is that no optical access to the reactor is needed and no limitations regarding the bubble load of the liquid phase exist. A disadvantage of this technique is, that the measured bubble sizes are not representing the actual diameter of the bubbles, but the chord lengths, as it is uncertain if a bubble is pierced right at the center or at the outside. The fact that only chord lengths are measured must be considered, while analyzing and discussing the results.

3.3 Experimental Setup and experimentation

This chapter is dealing with the experimental setup. All experiments were executed at a piloting scaled setup located in the experimental hall of the Hamburg University of Technology. A P&I diagram of the basic setup is displayed in *Figure 3-8*. All used measuring devices have been calibrated prior to their use.

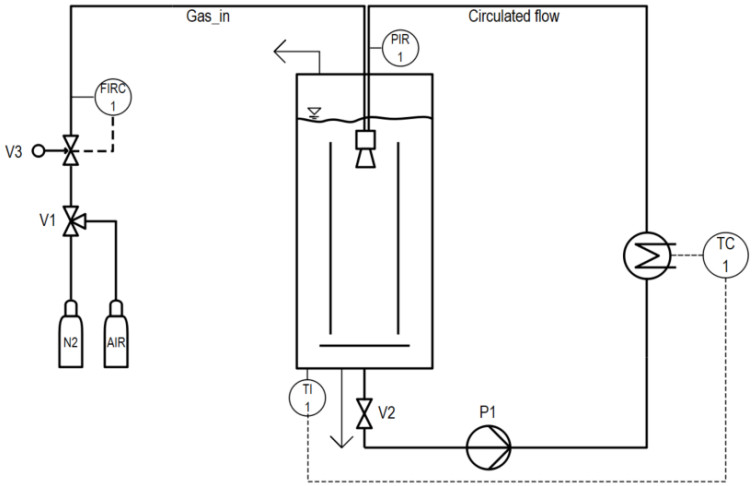

Figure 3-8: P&I diagram of the experimental setup in the experimental hall of the TUHH

The main component of this setup is the previously designed jet loop reactor with the derived dimensions, containing the draft tubes and the nozzle at the top. The jet loop reactor itself is a closed system. The water is getting sucked in by the pump at the bottom and reenters the reactor vessel through the nozzle at the top. In the P&ID this circuit is named circulated flow. The temperature of the water in the reactor is measured by a PT100 sensor (TI-1) placed in the water and is controlled by a Presto Julabo W40 thermostat (TC-1), using a plate heat exchanger EWT-BN4-10x30 containing 30 plates and an exchanging area of 0.33m^2 attached to

the circulated flow. The pressure loss of the nozzle is measured by a pressure sensor (PI-1) with a range of 0 to 2,5 bar. The pressure sensor is placed in direct proximity to the nozzle. The circulation is established by a Grundfos CRNE 5-8 centrifugal pump, with a maximum pressure head of 53 m and a flow rate of 5,7 m^3h^{-1}. The volume flux V_L is measured by the inductive flow meter ProMag30 of Endress+Hauser, located behind the plate heat exchanger and with an adequate inlet zone. All components are connected by a 13 mm hose on the pressure side behind the pump and with ½" Swagelok piping on the suction side prior the pump. For preventing a pressure increase in the reactor, the reactor lid contains a bore, allowing pressure equalization with the surrounding environment. The reactor, as it is used, is shown in *Figure 3-9*.

Figure 3-9: Test reactor in the experimental hall of the TUHH

3.3.1 Dynamic $\beta_L a$ and Bubble Size Measurements

For measuring the volume specific mass transfer coefficients $\beta_L a$, the previously described set up is complemented by a second liquid flow circuit, named measuring circuit. The corresponding P&I diagram is displayed beneath in *Figure 3-10*. This second circuit contains the centrifugal pump HTM10 by GemmeCotti with a maximum head pressure of 7 m and a maximum flow rate of 3.3 m^3h^{-1}. For measuring the liquid mass flow of the second circuit, a ProMass80F of Endress+Hauser is used, measuring the mass flow, the temperature and the density of the liquid. For determining the volume specific mass transfer coefficients $\beta_L a$, the oxygen concentration needs to be measured. Therefore, two PSt3 oxygen sensors combined with an OXY1-SMA unit, provided by PreSens Sensing, have been integrated within the measuring circuit directly before entering the reactor (O_2-IN) and directly after leaving it (O_2-OUT). The used oxygen sensors are explained in more detail in chapter 3.2

Besides measuring the volume specific mass transfer coefficient $\beta_L a$, this setup contains a fiber optical probe for measuring the chord lengths of the bubbles. The fiber optical probe of A2-Phontonics is placed in such way, that the tip of the probe is facing in the opposite direction of the flow. For validating the gained data with the fiber optical probe, a high-speed camera pco dimax HS2 with a Nikon-Nikkor 105 mm lens is used. The camera is filming the rising bubbles with an exposure time of 300 ms and a delay between each frame of 300 ms. As a back light, a LED panel is placed on the opposite site of the camera to offer a homogenous background light. All experiments are carried out with tap water, as the ProMag cannot measure the flow rate in distilled water. The temperature is kept constant at 20°C. The experiments are carried out at atmospheric pressure. The pressure loss of the nozzle, the liquid mass flow of the circulation and the mass flow of the sampling stream are recorded using a cRIO by National Instruments. In *Table 3-4* an overview of substance properties is listed.

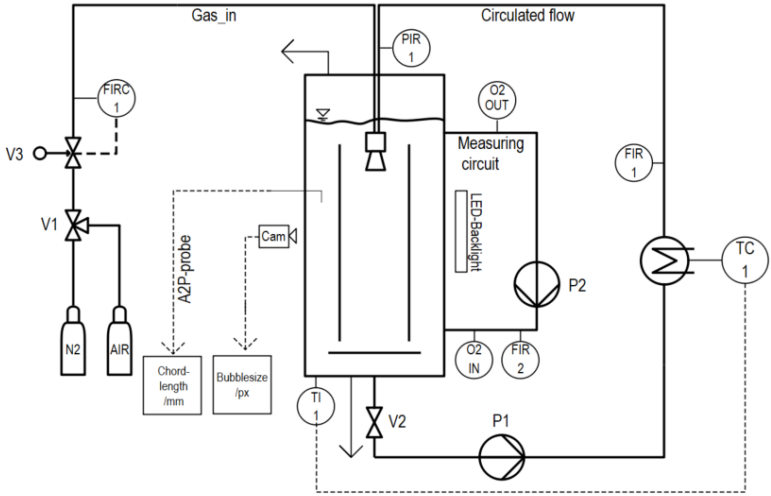

Figure 3-10: P&I diagram of the experimental setup used for the dynamic measuring of the $\beta_L a$ and the bubble sizes

The first part of the experimental work is the determination volume specific mass transfer coefficient $\beta_L a$ dynamically and the bubble sizes at different volume flow rates, gassing rates and two different draft tube configurations. The draft tube configurations investigated, are the standard, cylindrical draft tube made of acrylic glass and the flow optimized draft tube with the droplet shaped widenings printed in the SLA procedure. The used draft tubes are shown below in *Figure 3-11*.

Table 3-4: Substance properties of water and air under operating conditions at T = 20°C and p = 1,013 bar, the diffusion coefficient is calculated according to Henry's law [Dea99]

Property	***Symbol***	***H_2O***	***Oxygen***	***Unit***
Density	ρ	998	1.429	$kg \cdot m^{-3}$
Dynamic Viscosity	ν	$1{,}022 \cdot 10^{-3}$	$20.4 \cdot 10^{-6}$	Pa·s
Interfacial Tension	σ	$72.75 \cdot 10^{-3}$	-	$N \cdot m^{-1}$
Saturation Concentration	ρ*	-	9.1	$mg \cdot L^{-1}$
Diffusion Coefficient	D_{ij}	-	$1.9 \cdot 10^{-9}$	$m^2 \cdot s^{-1}$

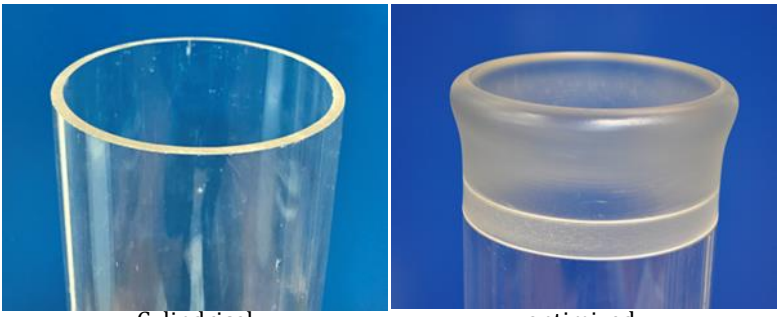

Cylindrical optimized

Figure 3-11: Investigated draft tubes: cylindrical draft tube made of acrylic glass and flow optimized SLA printed draft tube

Before each measurement, the oxygen is removed from the water in the reactor using nitrogen. When the oxygen concentration is close to 0% the measurements are started. All measurements are repeated once. The draft tubes are investigated at gassing rates of 0.05 $g \cdot s^{-1}$, 0.1 $g \cdot s^{-1}$,

0.15 $g \cdot s^{-1}$ and 0.25 $g \cdot s^{-1}$. Additionally, a gassing rate of 0.02 $g \cdot s^{-1}$ is applied for the standard draft tube. For each gassing rate, the liquid mass flow is varied, starting at the lowest stable operating point of the loop. At each operating point, the bubble sizes are measured, using the A2-Photonics probe, taking a sample size of 4000 bubbles. At the first test series investigating the standard draft tube, the bubbly flow is additionally filmed with the high-speed camera taking 1000 pictures at each operating point. The bubble sizes derived from the pictures are compared to the datasets of the A2-Photonics probe in the results. At the same time, the oxygen concentration is measured for each point, using the measuring circuit, taking a liquid mass flow rate of 2.4 $L \cdot min^{-1}$ in the measuring circuit. The recording of the oxygen concentration starts, when the oxygen of the prior experiment is entirely removed by the nitrogen and ends, when the concentration in the reactor reaches the saturation point. A list with the detailed operating points for all gassing rates is given in *Table 3-5*.

Table 3-5: Gassing rates for the dynamic $\beta_L a$ measurements and the determination of the bubble sizes

Gassing Rate /g·s⁻¹	0.05	0.1	0.15	0.25
Superficial Gas Velocity /mm·s⁻¹	1.8	3.6	5.3	8.9

3.3.2 Static $\beta_L a$ Measurements

For the static determination of the volume specific mass transfer coefficient $\beta_L a$, a second reactor is needed, which is used to strip the oxygen from a water reservoir. The oxygen free water from the reservoir is then pumped continuously through the investigated reactor. The reservoir is a second, larger jet loop reactor, located in the experimental hall at the TUHH and contains about 200 L of water. A WTW oxygen sensor controls the oxygen concentration. The used pump and the flow meter are the same than in the previous set up. For controlling the liquid level in the reactor and keeping it constant, a U-bent is used, which can be adapted to the different liquid levels by turning it sideways. Assuming, the liquid phase is ideally mixed, the oxygen outlet concentration is constantly sampled, shown on the left of the reactor vessel in the P&I diagram *Figure 3-12*. The second oxygen sensor is placed right in front of the reactor as in the previous set up.

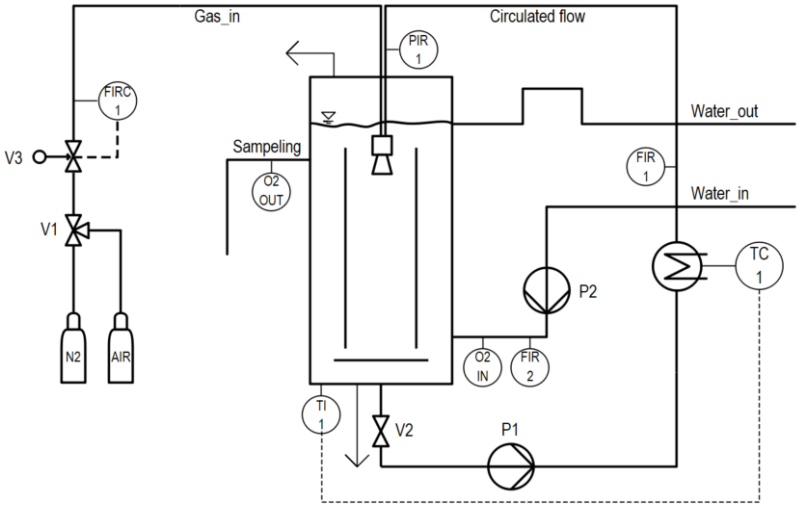

Figure 3-12: P&I diagram of the experimental setup for the static measuring of the $\beta_L a$

This setup is used for the second part of the experimental work, the stationary determination of the volume specific mass transfer coefficient $\beta_L a$. The operating conditions and used substances are the same as in the prior experiment. Again, all experiments are conducted twice. The stationary determination of the volume specific mass transfer coefficient $\beta_L a$ is only executed using the flow optimized 3D-printed draft tube (Type B), which has already been used for the dynamic method. For determining the $\beta_L a$ stationary, a second reactor is used to remove oxygen from the water reservoir. The observed reactor is operated at three different gassing rates ($0.05\ g \cdot s^{-1}$,$0.1\ g \cdot s^{-1}$ and $0.15\ g \cdot s^{-1}$) and the corresponding minimum liquid flow rates to establish a stable loop ($1.81\ m^3 \cdot h^{-1}$, $2.03\ m^3 \cdot h^{-1}$, $2.26\ m^3 \cdot h^{-1}$). The reactor is operated with a constant feed rate of $0.63\ m^3 \cdot h^{-1}$ from the reservoir. The oxygen concentration is measured right before the feed is entering the reactor and directly at the exit. Recording is started, when the oxygen concentration reaches a constant value.

4 Results and Discussion

In this section the results are displayed and discussed. The bubble properties and the volume specific mass transfer coefficients are determined for both draft tube types. The measured results of the volume specific mass transfer coefficient are validated for the flow optimized draft tube, applying a stationary determination method.

As described in chapter 2.4.3, the energy dissipation density has a significant impact on the mixing behavior, the mass transfer and the interfacial areas [Wie11]. Therefore, the results are plotted against the energy dissipation density P/V. This allows the characterization of the reactor in contrast to of different reactor types, by using the same specific measure. The mean energy dissipation density is calculated, based on the measured volume flows by rearranging (eq. 2.23). The results of the calculated energy dissipation densities are listed in the appendix at *Table A- 1*.

4.1 Determination of Bubble Properties

On the following pages the results of the experimental determination of the bubble properties are displayed and discussed. Measurements are conducted for the two mentioned draft tubes. Those draft tube configurations have been chosen, based on the gas hold-up measured in previous work. The results are graphically illustrated in *Figure 4-1* and show the gas hold-ups of the benchmark system with the cylindrical draft tube (filled symbols) and the flow optimized draft tube (open symbols) which was providing the best gas hold-up of all tested systems. In the illustration it can be observed that the flow optimized draft tube is providing a higher gas hold-up at any gassing rate. Though the trends are approaching each other with an increasing amount of gassing.

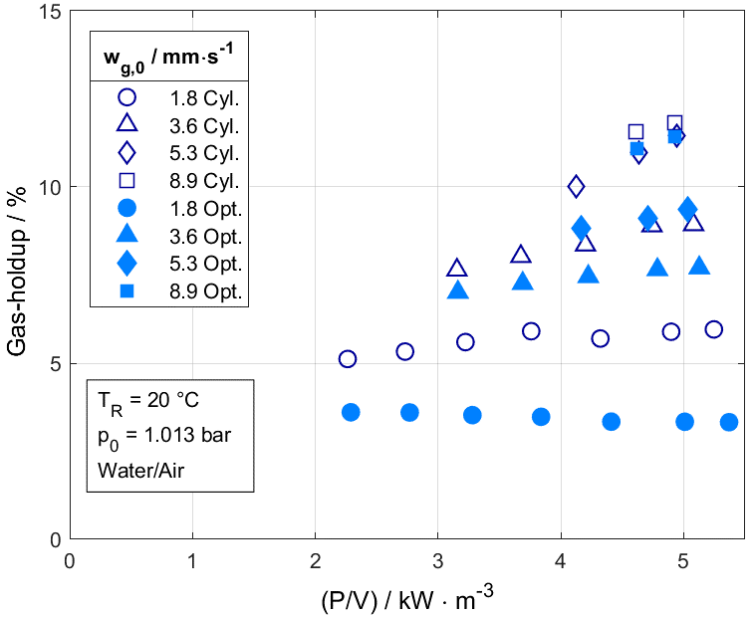

Figure 4-1: Results of the gas hold-up measurments performed in the a previous work at the IMS [Sch19]. Measurements are performed at 20 ° C and surrounding pressure of 1.013 bar in a water air system

This general trend indicates that the gas is kept in the system and is not degassing as fast, using the flow optimized draft tube. This assumption can be justified by looking at the trend of the gas hold-up at the lowest superficial gas velocity $w_{g,0}$ = 1.8 mm·s^{-1}. While the gas hold-up is reaching a maximum and is declining afterwards, using the cylindrical draft tube, it is constantly increasing with rising energy input, using the flow optimized draft tube. The increasing gas hold-up is an improvement of the process, if a reactor is used for chemical reactions, totally consuming a valuable gas while the gas is leaving the system not as easily. Though, if an inert component is present, it can accumulate in the circulating flow and is not getting entrained as often, resulting in a deteriorated performance of the reactor.

For the evaluation and a precise characterization of the observed jet loop reactor, the gas hold-up is a key parameter. Though further knowledge about the bubble characteristics, especially the bubble size, is needed. Therefore, the bubble size was measured with the A2-Photonics fiber optical probe. An exemplary dataset obtained with the fiber optical probe at an energy input of $P/V = 2.06$ kW·m^{-3} and a superficial velocity $w_{g,0} = 1{,}8$ mm·s^{-1} is provided in *Figure 4-2*, showing the chord length distribution q_0 (blue bars) and the cumulative chord length distribution Q_0 (red). The chord length is not equal to the bubble diameter, as the probe is usually not hitting the center axis of the bubble, as described in chapter 3.2.2.

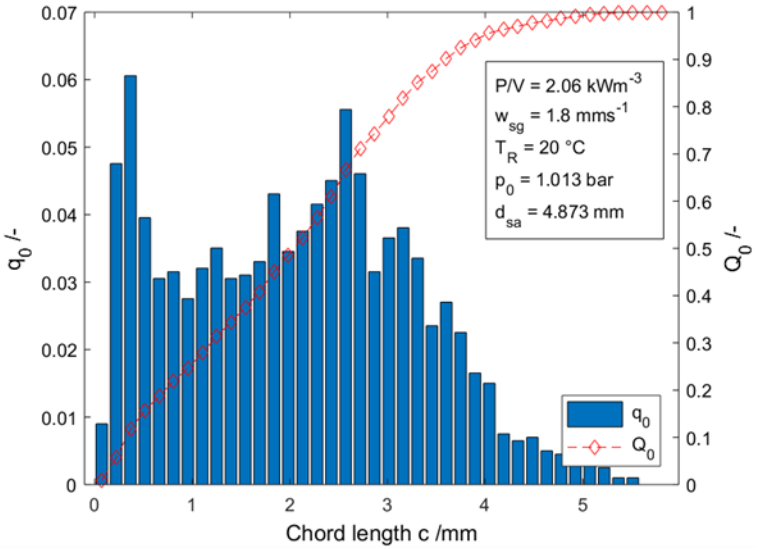

Figure 4-2: Chord length distribution measured with the fiber optical probe of A2-Photonics in the rising part of the jet loop reactor using the cylindrical draft tube

The analyzing tool of the measuring system provided by A2-Photonics is assuming, all bubbles are within a spherical regime. Although it reaches the system limits, when the bubbles have ellipsoidal, wobbling or unsettled shapes. For a first check, if the assumption of spherical bubbles, implied by the analysis procedure, is correct, the Sauter diameter based on the chord length C_{10}

$$d_{sa,sph} = \frac{3}{2} \cdot C_{10} \tag{4.1}$$

is calculated. The smallest bubble of 1.5 mm and greatest bubble of 6 mm detected in the bubbly flow and calculated by the system according to (eq.4.1) are compared to the *Grace* diagram in *Figure 4-3*.

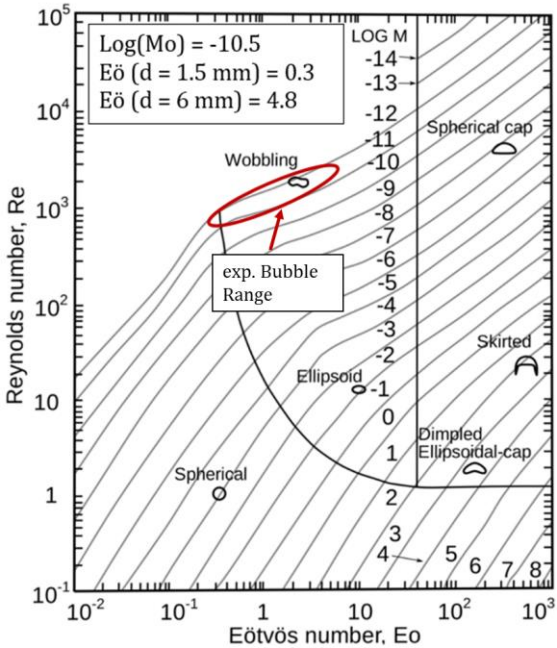

Figure 4-3: Grace diagram [Gra76] with highlighted range of bubbles according to the chord length distribution analyzed using the tool of the A2-Photonics probe

The marked positions indicate, that the spherical assumption, made by the analyzing tool, is not fulfilled and the bubbles tend to be in the wobbling regime instead. Therefore, the Sauter diameter of the bubbles cannot be determined, using the measurement technique directly. Instead, the obtained data is post processed by applying an alternative statistical analysis of the chord length distribution first proposed by *Liu & Clark.*

The backwards transformation of the chord length distribution into a bubble size distribution is done according to the work of *Liu & Clark* proposed in 1998*.* In their work, a statistical approach based on probability density functions for transferring chord length distributions (CLD) into bubble size distributions (BSD) is described in detail. The main idea of this approach is, that a chord length distribution is related to a bubble size distribution and the bubble size population distribution around the fiber optical probe. The probability density function

$$P_C(C|R) = P(r|R)\left|\frac{dr}{dy}\right| \tag{4.2}$$

is describing the likelihood of finding a chord length C for bubbles with a radius R [Liu98]. A detailed derivation of this probability function is given elsewhere [Liu98]. Applying the backwards transformation of *Liu & Clark* results in the bubble size distribution given in *Figure 4-4*. The knowledge about the bubble size distribution allows the calculation of the total surface S_{tot} and the total volume V_{tot} of the bubbles. Based on those calculated values the Sauter diameter is calculated

$$d_{sa,stat} = \frac{6 \cdot V_{tot}}{S_{tot}} = \frac{\pi \cdot d^3}{\pi \cdot d^2} \tag{4.3}.$$

The calculation of the bubble size distribution based on the probability functions and calculating the Sauter diameter, is performed using a self-developed MatLab script, which is based on the work of Liu & Clark [Liu98]. The used code, for transferring chord length information into bubble size information, is given in the appendix.

By looking at *Figure 4-4* it is clearly visible that the bubble size distribution is shifted to the right in comparison to the chord length distribution, corresponding to the expectations, that a spherical bubble is on average bigger than indicated by the device. This fact is underlined by taking a closer look at the Sauter diameter calculated by the statistical approach, which has a value of $d_{sa,stat}$ = 4.873 mm. The Sauter diameter calculated under the spherical assumption of the analyzing tool (eq. 4.1), only reaches a value of $d_{sa,aph}$ = 2.46 mm.

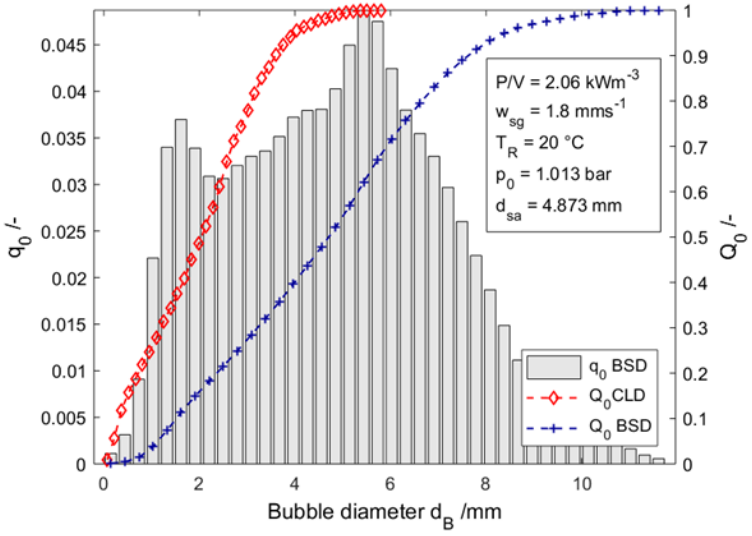

Figure 4-4: Bubble size distribution post processed using the statistical approach of Liu & Clark including the Q(0) distributions of the chord lengths (red) and the bubble sizes (blue)

For validating the statistical analysis, the bubble sizes for the cylindrical draft tube reactor are also measured using a high-speed camera. For each operating point 1000 pictures of the rising bubbles were taken. At each operating point, the major and minor length of 200 or more elliptical

shaped bubbles was measured. For transferring the measured pixel values into a common unit of length, a target picture is taken, resulting in a ration of 190px/10mm with an accuracy of ±2 px. Under assumption of rotational symmetry and knowing the actual lengths of the major p and minor s axis of each analyzed bubble, the surface and volume of each bubble is calculated. The information is used for calculating the Sauter diameter

$$d_{sa,pic} = \frac{6 \cdot \sum \frac{4}{3}\pi \cdot p^2 \cdot s}{\sum 2\pi \cdot p \left(m + \frac{s^2}{\sqrt{n^2 - s^2}} \cdot arsinh\left(\frac{\sqrt{p^2 - n^2}}{s} \right) \right)} \qquad (4.4).$$

The error of the calculated Sauter diameter $d_{sa,pic}$ is within a range of ± 0.105 mm and is calculated according the to equations and rules given in chapter 5.1.1. Besides yielding information about the Sauter diameter, the pictures approve the prediction regarding the bubble shape regime being wobbling, which can be seen in *Figure 4-5* showing the bubbly flow at two flow conditions in the cylindrical reactor.

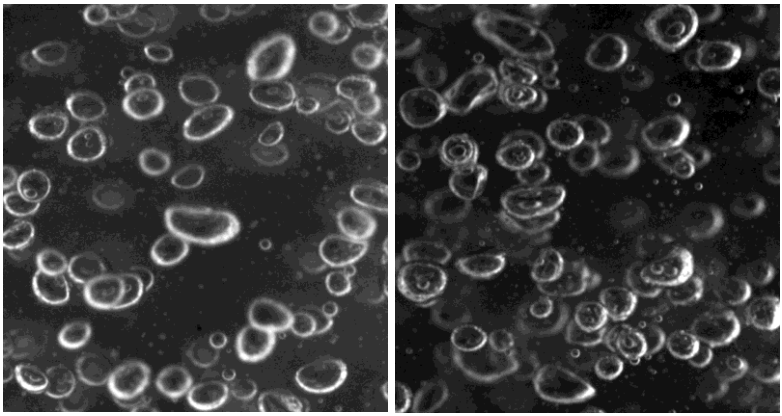

(a) (b)

Figure 4-5: Bubbly flow at an energy input of P/V = 2.06 kW·m^{-3} and a superficial gas velocity of $w_{g,0}$ = 1.8 mm·s^{-1} (a); P/V = 4.82 kW·m^{-3} and $w_{g,0}$ = 8.9 mm·s^{-1} (b) obtained with the cylindrical draft tube

The experimentally obtained bubble Sauter diameters, using the cylindrical draft tube, are displayed in *Figure 4-6*. The plot indicates that the Sauter diameters $d_{sa,sph}$ computed by the probe directly (red), are within a range of 2 mm to 3 mm. They are underestimated, compared to the information provided by the camera (black). The Sauter diameter $d_{sa,pic}$ according to the camera, is within a range of 5.5 mm to 7 mm. The post processing of the direct measured data by the statistical approach of *Liu & Clark(blue)* shows Sauter diameters $d_{sa,stat}$ in a range of 4 mm to 6 mm and is much closer to the values based on the camera footage. The data displayed in this and the following scatter plot is given in *Table A- 2* in the appendix.

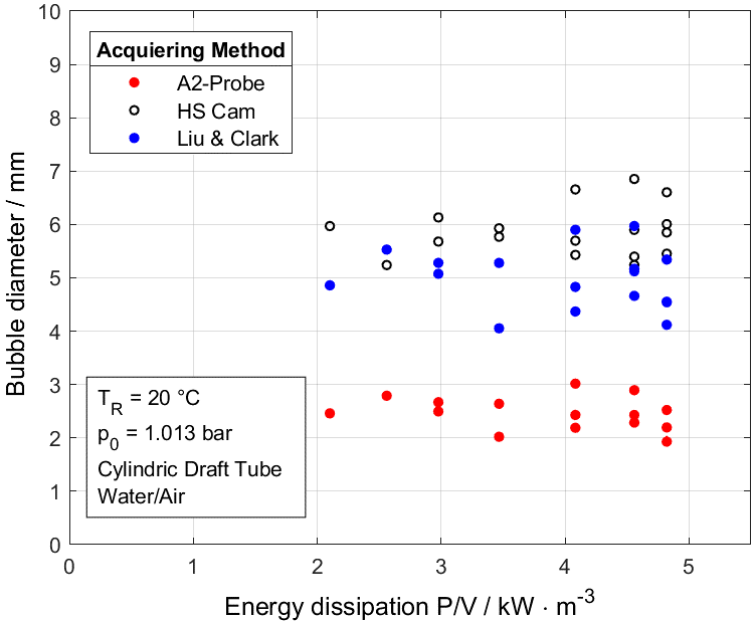

Figure 4-6: Scatter plot comparing the bubble Sauter diameters obtained by the A2-Phonoics code (blue) , the statistical analysis of Liu & Clark (red) and the high speed camera (black) for the cylindrical draft tube

The plot in *Figure 4-7* compares the statistically analyzed Sauter diameters $d_{sa,stat}$ of the cylindrical draft tube (red) and the flow optimized draft tube(blue). The plot provides a qualitative perspective on the bubble sizes and shows that the bubbles in the flow optimized draft tube tend to be larger. The Sauter diameter of the bubbles, measured in the cylindrical draft tube, are within a range of 4 mm to 6 mm, whereas the bubbles in the flow optimized draft tube are in a range of 6 mm to 9.3 mm. A possible explanation for this behavior, is a reduced shear and a lower energy loss at the rounded edges of the flow optimized draft. The lower shear might prevent the bubbles from being split into smaller fractions and the mean bubble diameter is increasing over time due to coalescence effects, until reaching an equilibrated state.

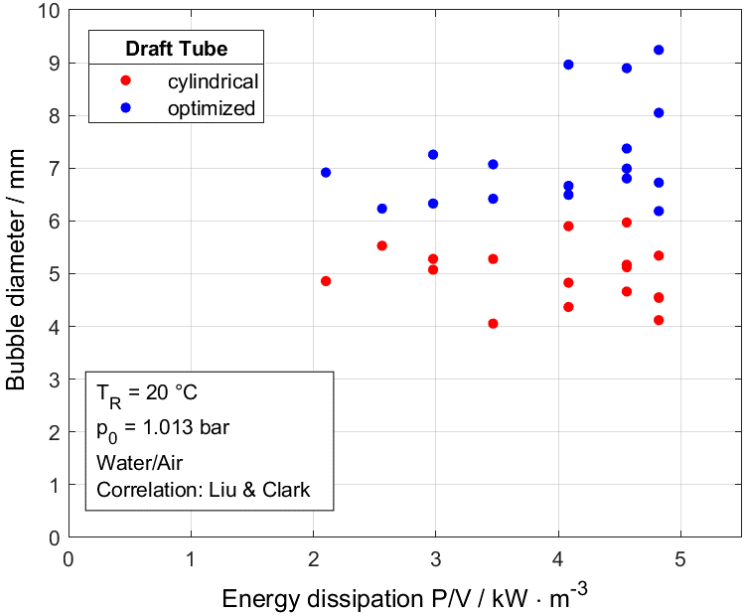

Figure 4-7: Scatter plot of the Sauter diameters for the cylindrical draft tube (A -red) and the flow optimized draft tube (B-blue)

The results of the first part of the experimental work show, that the overall gas hold-up increases, using the flow optimized draft tube; though the bubble size increases as well, compared to the cylindrical stand draft tube. An explanation for this behavior is, that the flow conditions are changed, applying the drop shaped widenings. Therefore, the gas is kept in the system and is not degassing with the same speed. The flow optimized draft tube also effects the overall trend of the bubble size. Looking at the experimental results, the bubbles sizes tend to be larger for the flow optimized draft tube. This coherence is reasoned again by the flow conditions. As the flow is guided around the rounded edges, the occurring shear is probably lower than at the sharp edge of the cylindrical draft tube. The reduction of the shear is preventing bigger bubbles from getting torn apart, enhancing the effect of coalescence and the bubble size is increasing.

4.2 Determination of Mass transfer coefficient

Knowing the volumetric liquid-phase mass transfer coefficient $\beta_L a$ of gas-liquid reactions, is of great importance for the chemical and the biochemical industry and allows to optimize reactors according to their mass transfer capabilities. Therefore, several methods for measuring the mass transfer have been developed in the past. As several effects affect the local mass transfer, it is difficult to measure the mass transfer exactly. Instead, the mean mass transfer rate of a system is determined. For this work, two methods for measuring the volume specific mass transfer coefficient are applied, the dynamic adsorption-desorption method and a stationary method by feeding oxygen free water in the reactor.

4.2.1 Dynamic Adsorption/Desorption Method

The goal of this measurement series is the determination of the volume specific mass transfer coefficient by using a dynamic adsorption/desorption method. It is widely used for determination and is known for its simple and easy operation principle. At first the dissolved oxygen in the observed liquid is stripped out by sparging nitrogen into the reactor. When the oxygen concentration becomes neglectable, the reactor is gassed with air and the oxygen concentration c increases over time t, allowing to set up an oxygen balance

$$\frac{dc}{dt} = \beta_L a \cdot (c^* - c) \qquad (4.3),$$

where c* represents the saturation concentration of oxygen in the equilibrated state and integration yields

$$-\beta_L a \cdot t + constant = ln(c^* - c) \qquad (4.4),$$

allowing the determination of the volume specific mass transfer coefficient $\beta_L a$ as the negative slope of the resulting function [Nak80].

The approach is based on three assumptions [Nak80]:

- The liquid phase is perfectly mixed
- The driving potential for mass transfer is uniform throughout the reactor
- The response time of the oxygen probe used, is sufficiently fast

Prior to the measurements of the oxygen concentration trends at the different operating points, the maximum saturation concentration c* at the equilibrated state is measured at the reactor outlet, using the same setup used for the dynamic measurements. Data for the saturation concentration is acquired at the operating temperature of T = 20 °C for a time period of 30 minutes. The resulting values of the oxygen saturation concentration and species densities are given in *Table 4-1* and are used for all following calculations. Although the oxygen probe is calibrated prior to the experiment, the saturation concentration c* is above 100%. This effect is due to the slightly higher hydrostatic pressure at the bottom of the reactor, resulting in a slightly higher saturation concentration and the good mixing of the reactor. As the oxygen is not dissolving from the water fast enough until it reaches the probe, the measured saturation concentration has a value of 102.16 % or 0.288 mmol·L^{-1}.

Table 4-1: Maximum oxygen saturation concentration and species density measured with the PreSens Oxy SMA system

-	***Saturation Concentration / %***	***Species Concentration c /mmol·L^{-1}***
Mean value	102.16	0.2888
Standard deviation	0.0714	0.00020
Maxima	102.36	0.2893
Minima	101.93	0.2881

The oxygen saturation process is measured and analyzed twice for each operating point and each reactor design. An example of the observed trends is shown in *Figure 4-8*. Afterwards it is switched from stripping with nitrogen to active gassing with compressed air. The oxygen concentration in the reactor is increasing over time and is converging against the concentration at the equilibrated state. In the graphic it is visible that the gradient changes over time. For evaluating the volumetric mass transfer coefficient, the section of the trend is chosen, which is most linear. In case of the actual experiments this linear section with an almost constant gradient is in between 20% and 70% of oxygen concentration.

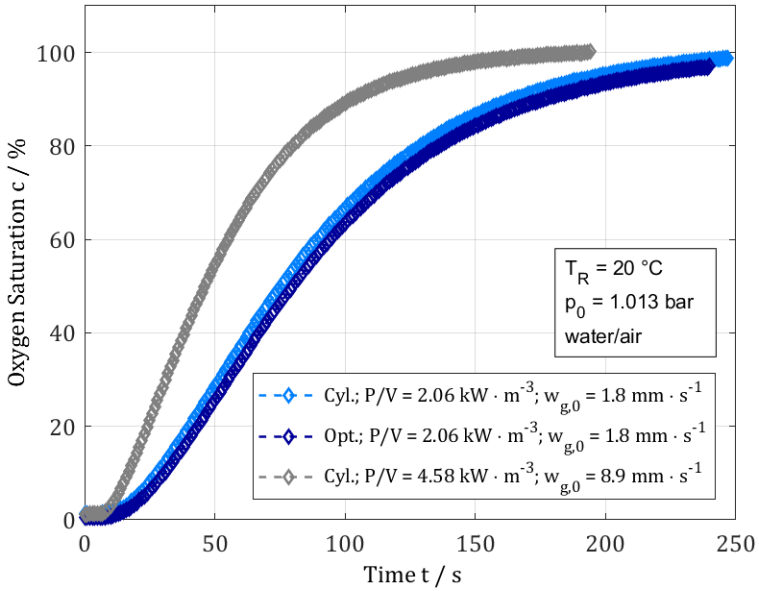

Figure 4-8: Trend of the oxygen saturation for three measurement points using the cylindrical draft tube (Cyl.) and the flow optimized draft tube (Opt.) at different gassing rates and energy inputs

By applying (eq. 4.4) and inserting the measured maximum oxygen saturation the trend is linearized between an oxygen saturation of 20% to 70%. *Figure 4-9* shows exemplary, the linearized trend of the measurement at an energy input of 4.58 kW and a superficial gas velocity of $w_{g,0}$ = 8.9 mm·s^{-1}. The slope of the resulting graph is equivalent to the volume specific mass transfer coefficient. The arising errors of the two measurement campaigns, are within a range of ± 15 %, looking at the cylindrical benchmarking system and in between ± 20 %, using the flow optimized draft tube. Those errors are within a common range for the determination of the volume specific mass transfer coefficient, using the adsorption/desorption method. A detailed description how those error values are derived, is in chapter 5.1.2.

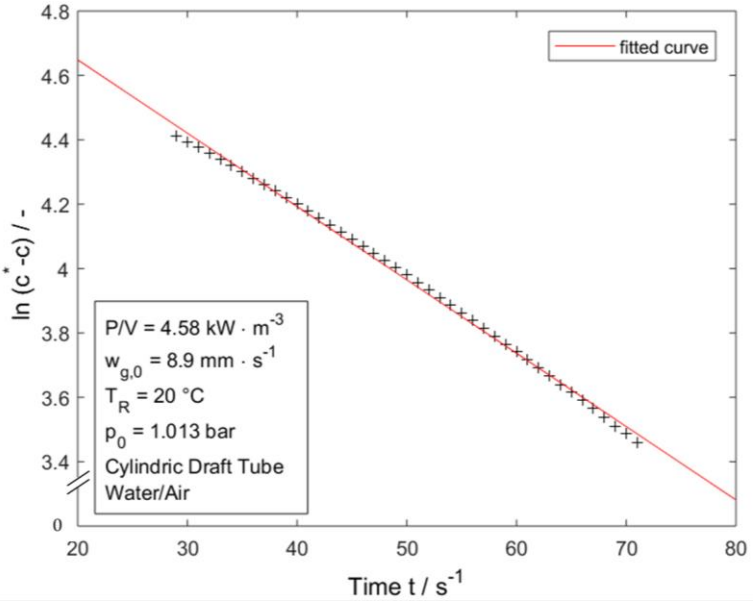

Figure 4-9: Linearized plot used for the determination of the volume specific mass transfer coefficient.

In *Figure 4-10* the mean volume specific mass transfer coefficients measured with the cylindrical draft tube (A-filled) and the optimized draft tube (B-open). The corresponding values, including the maximum and minimum deviation, are given in *Table A- 3* for the cylindrical and in *Table A- 5* for the optimized draft tube. The mean volume specific mass transfer coefficients, using the cylindrical draft tube, are within a range of β_{La} = 49.8 h^{-1} and β_{La} = 79.6 h^{-1} and within the borders of β_{La} = 49.2 h^{-1} and β_{La} = 91.9 h^{-1} applying the flow optimized draft tube. Both measurements show a deviation of about ± 20%. A detailed description of the error estimation is given in chapter 5.1.2. For better presentability the measurement errors are not given in the plot but are listed for both draft tubes in *Table A- 3 and Table A- 5* in the appendix.

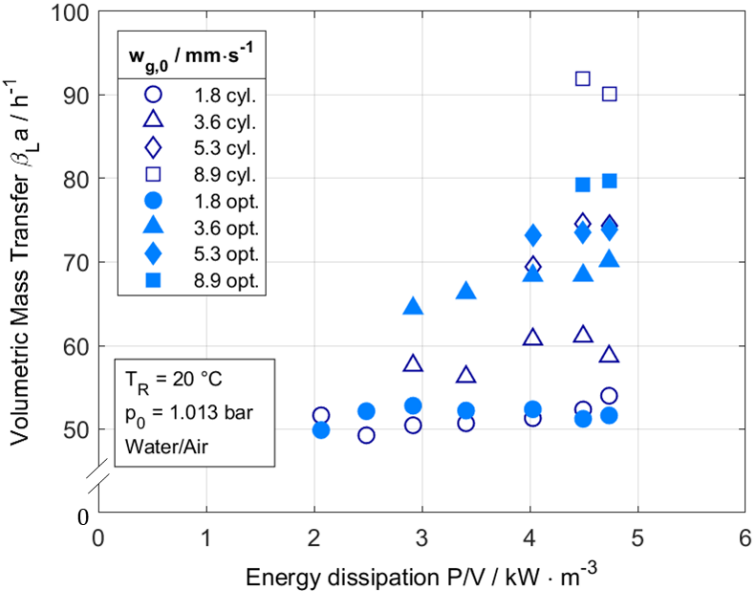

Figure 4-10: Comparison of the mean volume specific mass transfer coefficients β_{La} obtained using the cylindrical (filled) and the flow optimized (open) draft tube

By looking at the plot, two tendencies can be observed for both draft tubes. On one side, the volume specific mass transfer is reaching higher values for an increasing gassing rate. On the other hand, the value is staying almost at the same level while increasing the energy dissipation. This observation is corresponding to literature [Far07]. Besides the overall trends, the plot is showing three other occurrences. While the volume specific mass transfer is within the same range at the lowest superficial gas velocity $w_{g,0}$ = 1.8 mm·s^{-1} for both draft tubes, there is a changing behavior at the remaining operation points. If the gassing rate increases to superficial velocities of $w_{g,0}$ = 3.6 mm·s^{-1} and $w_{g,0}$ = 5.3 mm·s^{-1}, the volume specific mass transfer coefficient is better with the cylindric draft tube. Though this circumstance changes at the highest gassing rate and the flow optimized draft tube is providing a better mass transfer, compared to the cylindrical draft tube.

Since the mass transfer coefficient $\beta_L a$ is dependent on the area a and the mass transfer coefficient $\beta_{L,}$ a change of one of those values, is resulting in a changing volume specific mass transfer performance. As both measurement campaigns are proceeding at the very same conditions, i.e., regarding temperature and pressure and no additionally applied surface-active agents, it is assumed that the mass transfer coefficient β_L stays roughly constant. Therefore, the differences in the volume specific mass transfer coefficient are most likely caused by a smaller interfacial area. The interfacial areas at the different operating points are generally calculated by

$$a = \frac{6 \cdot \epsilon_G}{d_{sa}} \qquad (4.5),$$

considering the gas hold-up and the Sauter diameter. For both systems the Sauter diameters using the spherical assumption $d_{sa,sph}$ and the statistical analysis $d_{sa,stat}$ are available. Because of their closer match to the camera-based measurements at the cylindrical draft tube, the Sauter diameters, using the statistical approach, are used for calculating the interfacial areas. In *Figure 4-11* the mean interfacial areas for each gassing rate and both draft tube systems are plotted. The values are plotted with their

maximum/minimum deviation. The corresponding values of each gassing rate and the different draft tubes are given tabularly in *Table A- 7*.

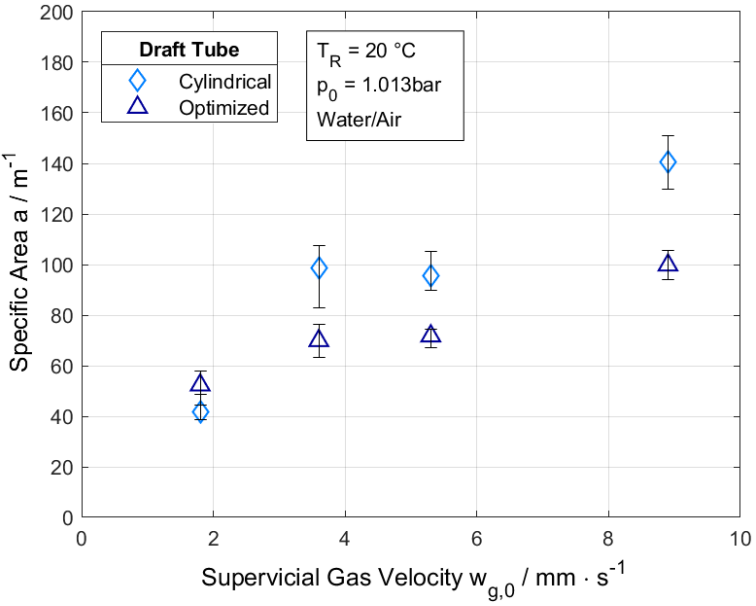

Figure 4-11: Mean interfacial areas at the different gassing rates for the cylindrical draft tube (diamond) and the optimized draft tube (triangle)

The trends of the interfacial areas visible in the plot show a similar behavior like the measured volume specific mass transfer coefficients in *Figure 4-10*. The interfacial area is almost of the same size at the lowest superficial velocity of $w_{g,0}$ = 1.8 mm·s^{-1}, which corresponds to the similar volume specific mass transfer at this gassing rate for both draft tubes. Although the interfacial areas are smaller, using the optimized draft tube at the remaining gassing rates. This is a result of the increasing bubble size (compare *Figure 4-7*) and even the gas hold-up is increasing simultaneously; using the flow optimization (compare *Figure 4-1*), the specific area is overall decreasing. The smaller interfacial area is directly connecting to

the lower volume specific mass transfer coefficient at the middle two gassing rates, but not to the higher volume specific mass transfer at the highest gassing rate with a superficial velocity of $w_{g,0}$ = 8.9 mm·s^{-1}. As the determination of the volume specific mass transfer is burdened with an error of about ± 20% for both draft tubes (compare *Table A- 3* and *Table A-5*), a measurement error rather than an actual increasing volume specific mass transfer at the highest gassing rate is the most likely explanation.

In conclusion the volume specific mass transfer tends to be smaller using the flow optimized draft tube, those values will be validated in the next chapter. Considering the measurement uncertainties, the change of volume specific mass transfer is not of significant magnitude.

4.2.2 Stationary Method

For validating the results of the dynamic determination method, the volume specific mass transfer coefficient is also determined, using a stationary measuring method, by feeding oxygen free water in the reactor. The measurements are carried out at three operating points and are used only for validating the dynamically measured data. The results of this second measurement campaign are displayed and discussed in the following.

Measuring the volume specific mass transfer coefficient stationary, enables the calculation of the transferred oxygen, since the oxygen balance is closed. The reactor is operated at the desired operation points and a constant feed flux with oxygen free water is running through the system. When a stationary point is reached, the oxygen concentrations at the inlet and the outlet are recorded, allowing to calculate the volume specific mass transfer coefficient

$$\beta_L a = ln\left(\frac{\rho_G^* - \rho_{G,o}}{\rho_G^* - \rho_{G,i}}\right) \cdot \frac{\dot{V}_L}{V_R} \qquad (4.12).$$

As the values are measured over a certain time period, the resulting volume specific mass transfer coefficient is an averaged value over time. Besides determining the mass transfer coefficient, this method provides all necessary information for calculating the transferred oxygen by

$$\dot{m} = \beta_L a \cdot V_R \cdot (\rho_{out} - \rho_{in}) \qquad (4.13).$$

All measurements of this campaign are done at the same system temperature and pressure as the dynamic measurements. The determined volume specific mass transfer coefficients, measured for the three operating points, are listed in *Table 4-2*, including the corresponding errors.

Table 4-2: Results of the stationary determination of the volume specific mass transfer coefficient

Energy Dissipation P/V / kW·m⁻³	***Volumetric Mass Transfer Coefficient $\beta_L a$ /h⁻¹***	***Max. Deviation / h⁻¹***	***Min. Deviation / h⁻¹***
2.07	44.3	1.65	1.08
2.92	64.6	2.52	2.47
4.03	79.2	7.13	3.15

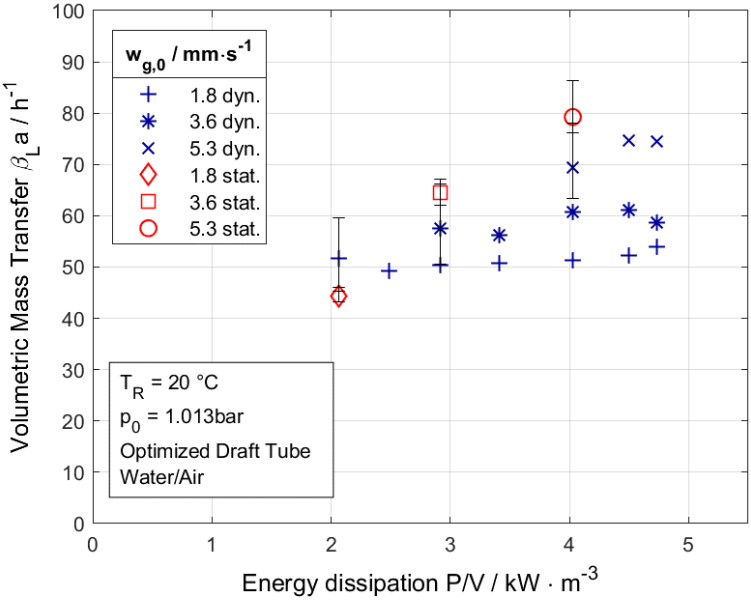

Figure 4-12: Comparison of the dynamically measured values (blue) to the stationary measured values (red) at the same operating conditions for validation reasons

Figure 4-12 illustrates the volume specific mass transfer coefficient, measured dynamically, marked blue, and stationary, marked as red diamonds. Both values are only slightly apart and within the range of measurement errors. As both values show a satisfying agreement, the results of the dynamic adsorption/desorption method are confirmed.

A major advantage measuring the volume specific mass transfer coefficient with a stationary method is that the oxygen balance for the observed system is closed. As the oxygen concentration of the feed and the concentration in the outlet are known, the transferred mass flux of oxygen from the gaseous into the liquid phase can be calculated, applying (eq. 4.13). The results and the related errors are given in *Figure 4-13*. The derivation of the errors as well as the error sources, will be explained in chapter 5.1.3.

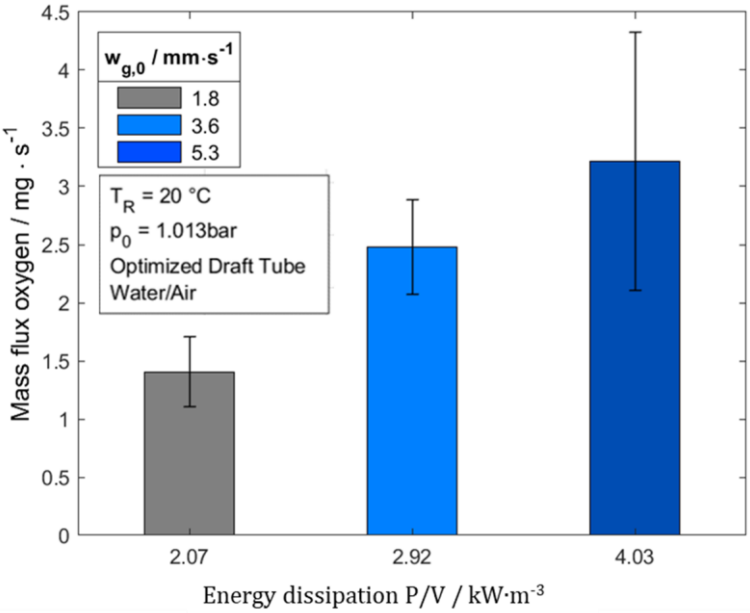

Figure 4-13: Mass flux of oxygen at the different energy dissipation densities

4.3 Data Modeling

Predicting the performance of reactors is important for all fields of usage. Therefore, different correlations describing reactor systems have been developed in the past. Two of these correlations will be compared to the measured data of the flow optimized reactor on the following pages.

4.3.1 Correlation of Energy Dissipation Rate

At first the measured data is compared to a correlation proposed by *Farizoglu* in 2007 [Far07]. The author is using an approach, based on the assumption made by *Zehner* [Zeh05], who stated, that the volume specific mass transfer coefficient is proportional to the introduced gas flux to the power of b. On this basis, the energy dissipation density and the gas flux are correlated by the relation

$$\beta_L a = C \cdot \left(\frac{P}{V_R}\right)^a \cdot (\dot{V}_G)^b \qquad (4.7).$$

In case of the chosen correlation of *Farizoglu,* the general construction yields

$$\beta_L a = 23.39 \cdot \left(\frac{P}{V_R}\right)^{0.17} \cdot (\dot{V}_G)^{0.8} \qquad (4.8).$$

In *Figure 4-14* this correlation is plotted for the four different gassing rates and is compared to the measured data, applying the cylindrical draft tube. The equivalent plot comparing the correlation with the flow optimized draft tube, is given in the appendix in Figure A- 8 . By comparing both trends, the correlation lies within the same order of magnitude and shows the same trend to increase with energy dissipation. It is matching the data for the middle two gassing rates already up to a satisfying degree but is underestimating the volumetric mass transfer at the lowest gassing rate by about 20% and overestimating at the highest rate by about 50%. Since the general trend of the volumetric mass transfer with increasing

superficial gas velocity is described properly, the basic appearance of this correlation is taken and refitted to the measured data.

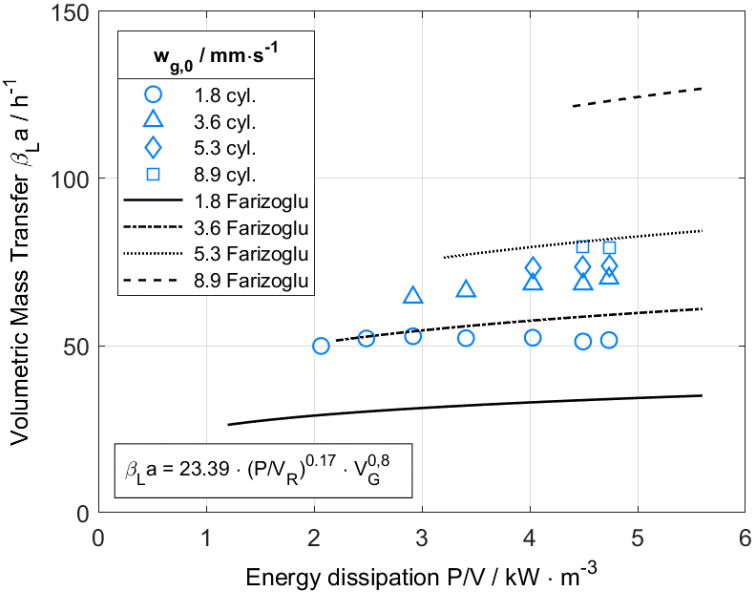

Figure 4-14: Measured data points of the cylindrical draft tube (light blue), compared to the correlated values by Farizoglu (black)

The new correlation, valid for a two-phase water/air system, is refitted individually for each reactor setup. The general appearance of the correlation is not changed; just the exponents and the constant are reevaluated. The correlated exponents and constants are given in *Table 4-3*. The size of the exponents indicates that the influence of the gassing rate is greater than the influence of the energy input, which is in good agreement with the trend of the measured data. The exponents and the constant are fitted, using the entire available data of each draft tube. The resulting correlations are compared to the measured data using the cylindrical draft tube in *Figure 4-15* and the optimized draft tube in *Figure 4-16*. Both self-fitted correlations show a good agreement with all measured data sets and have a maximum deviation of ± 10%.

Table 4-3: Exponents and constants for the refitted correlation

Exponent	***Cylindrical Draft Tube***	***Optimized Draft Tube***
C	0.17	0.4
a	0.14	0.05
b	0.26	0.34

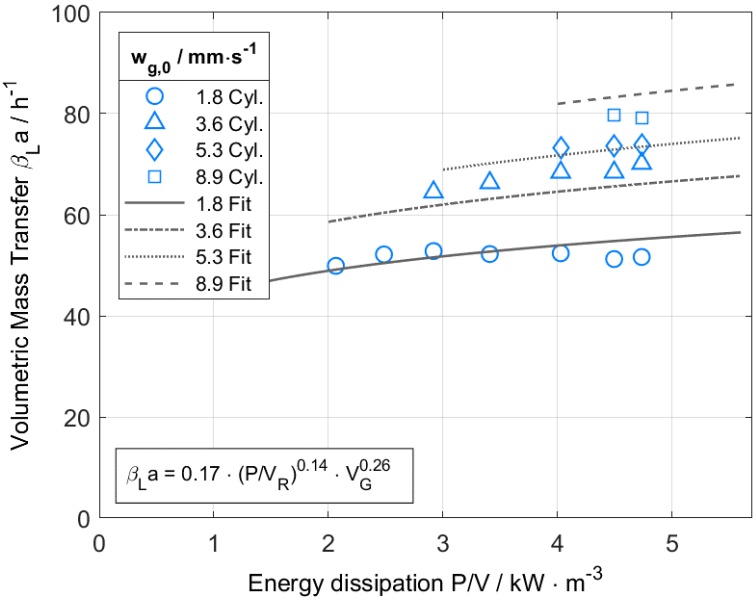

Figure 4-15: Refitted correlation based on the Energy dissipation density (grey) compared to the measured values using the cylindrical draft tube (light blue)

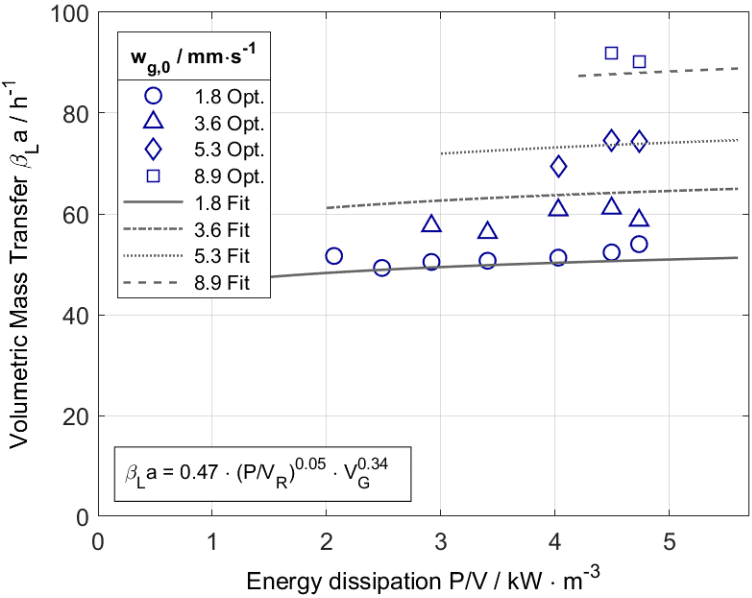

Figure 4-16: Refitted correlation based on the Energy dissipation density (grey) compared to the measured values using the optimized draft tube (dark blue)

If the correlations are compared to each other, the slope of the correlation for the cylindrical draft tube is steeper than the slope using the flow optimized draft tube. As both correlations fit the measured data with a similar deviation, this indicates that the energy dissipation is influencing the volume specific mass transfer at the cylindric draft tube stronger than at the optimized draft tube. Though the influence of the energy dissipation is bigger at the cylindrical draft tube, the dominating parameter is the gassing rate.

4.3.2 Sherwood Correlation

Besides correlating the volume specific mass transfer coefficient directly, Sherwood-correlations are popular. The major difference, compared to the first used correlation, is the ability of Sherwood correlations to estimate the conditions, based on dimensionless numbers and therefore allow scaling of reactor systems. As it is often difficult to measure for example the interfacial area present in jet loop reactors, most correlations in literature use an adapted Sherwood number, which is introduced in chapter 2.1 as the industrial Sherwood number Sh_{ind}. Considering this adapted Sherwood number, *Jamshidi* [Jam01b] proposed a correlation

$$Sh_{ind} = 1.76 \cdot Sc^{0.5} \cdot Re_T^{0.99} \cdot Fr^{0.5} \cdot Mo^{-0.06} \cdot \frac{0.15 + 1.05 l_D}{l_D + h_N} \qquad (4.10),$$

which was fitted for downstream air/water jet loop reactors in dependency of different positions of the nozzle above the draft tube. The values resulting from this correlation for the four different gassing rates, which correspond to four Froude numbers, are given graphically in *Figure 4-17*. At first glance it is obvious, that this correlation is overestimating the measured data at any time more than one order of magnitude. A possible explanation is a different reactor set up, using a draft tube with a ratio of just $d_D/d_R = 0.372$, instead of a draft tube with equal cross-sectional areas resulting in $d_D/d_R = 0.71$ as was used in the actual study.

As the most other correlations in literature are having a very similar appearance, the general approach of *Jamshidi* [Jam01b] is slightly changed for calculating a new correlation based on the acquired data. The last term in the correlation of *Jamshidi* [Jam01b] is varying the height of the nozzle above the draft tube. As the position of the nozzle is not changed and therefore no datasets are available for fitting a correlation containing this term, this term was neglected. The refitted correlation has the general appearance of

$$Sh_{ind} = C_1 \cdot Re_N^{\beta} \cdot Sc^{\gamma} \cdot Fr^{\kappa} \cdot Mo^{\zeta} \qquad (4.11),$$

and fitting the acquired data, yields the exponents and constants for the different draft tubes, listed in *Table 4-4*.

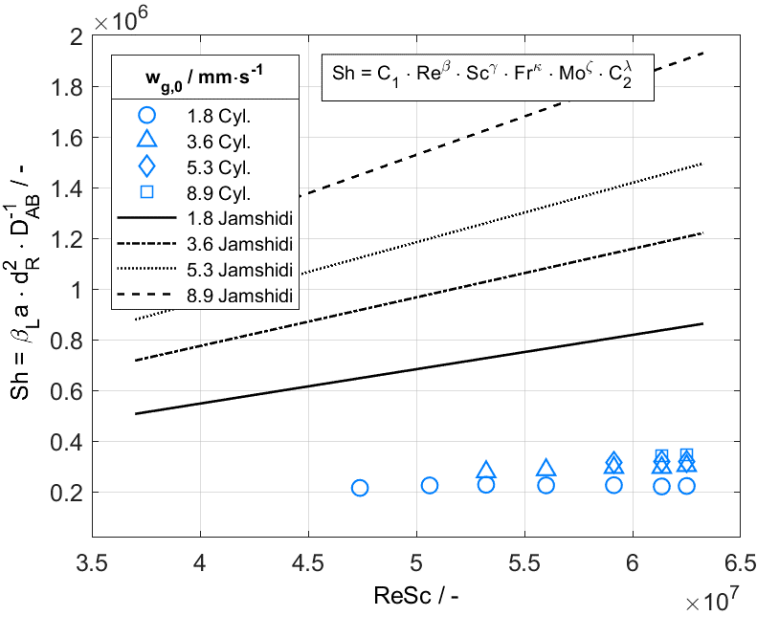

Figure 4-17: Industrial Sherwood number in dependency of (ReSc) for four different gassing rates (grey) compared to the measured values applying the cylindrical draft tube (light blue)

The refitted correlations for both draft tubes show again good accordance with the measured data. The deviation from the data lies within an error of ±10%. The resulting curves, applying the correlation for the cylindrical draft tube, are displayed in *Figure 4-18*. The results of the flow optimized draft tube in *Figure 4-19* .

Table 4-4: Exponents and constants for the refitted Sherwood correlations

Exponent	***Cylindrical Draft Tube***	***Optimized Draft Tube***
C_1	3.23	$3.3 \cdot 10^{3}$
β	0.43	0.24
γ	1.25	0.58
κ	0.26	0.34
ζ	$5 \cdot 10^{-5}$	$2 \cdot 10^{-4}$

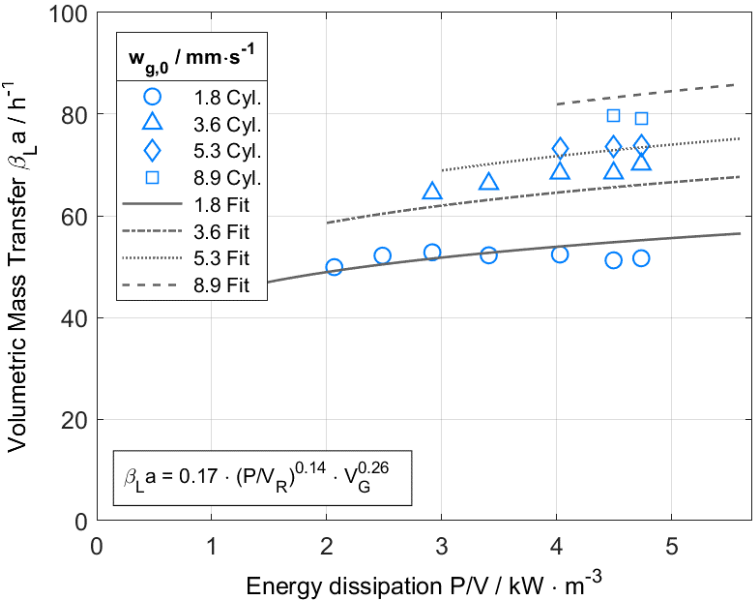

Figure 4-18: Correlation of industrial Sherwood number (grey) compared to measured values with the cylindrical draft tube (light blue)

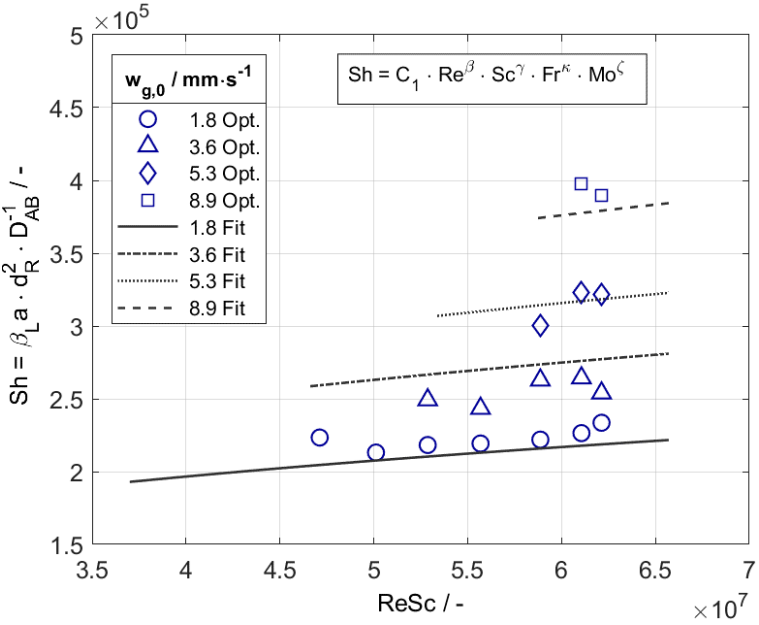

Figure 4-19: Correlation of industrial Sherwood number (grey) compared to measured values with the optimized draft tube (dark blue)

If the correlations are compared to each other, the slope of the correlation for the cylindrical draft tube is again much steeper than the slope using the flow optimized draft tube. It follows that an increasing energy dissipation is influencing the industrial Sherwood number and therefore the volume specific mass transfer coefficient $\beta_L a$ stronger, while using the cylindrical draft tube. Nevertheless, the gassing rate stays the dominating parameter at both draft tubes.

For correlating the measured volume specific mass transfer coefficients, two approaches are used. Both refitted correlations, one based on the energy dissipation and the other on the Sherwood number, show a good agreement with the measured values. As both correlation approaches are depending on directly measurable quantities, they are easy to apply.

Therefore, it is only depending on the application, which correlation is used. In case only the volume specific mass transfer coefficient is the aimed quantity, the correlation based on the energy dissipation provides a fast result. If the correlation is used for scaling the reactor system, the Sherwood correlation is the better option.

4.4 Results Summary

In the previous chapter, the results have been displayed, evaluated and discussed. In this chapter all information is reflected and summarized. The main dependencies found and elaborated upon in this thesis, are illustrated in *Table 4-5*.

Table 4-5: Dependencies of the measured quantities for different operating parameters

-	***Gas Hold-up*** ε_G ***/%***	***Sauter Diameter*** d_{sa} ***/ m***	***Mass Transfer Coefficient*** $\beta_L a$ ***/ h^{-1}***
$w_{g,0}$**: ↑**	↑	↑	↑
P/V: **↑**	↗	↓	↗

The bubble size and shape in the reactor system are mainly depending on the gassing rate and the energy input. In the observed system the bubbles tend to be of ellipsoidal shape. With increasing gassing, the bubbles are getting larger, while an increase in the energy input results in a decreased bubble size. Besides these effects, the bubbles are generally larger in the flow optimized reactor, which is probably caused by changing flow conditions, which seem to encourage the process of coalescence and/or hinder the dispersion into smaller bubbles. In contrast to the bigger bubbles the gas hold-up, especially at lower gassing rates, is increased by the flow optimization. The volume specific mass transfer coefficient $\beta_L a$ is deter-

mined for both draft tubes at four different gassing rates. With an increasing gassing rate, the mass transfer coefficient is increasing as well. The gassing rate is determined as the dominating factor for improving the mass transfer rate in the JLR. The influence of the energy input is rather small and must be increased only, to maintain the loop circulation at higher gassing rates. For the flow optimized draft tube, the influence of the energy input on the mass transfer coefficient is rather small and the volume specific mass transfer depends almost solely on the gassing rates. Compared to the values available from literature, shown in *Figure 4-20*, measured at superficial gas velocities from $w_{g,0}$ = 0.25 – 6 cm·s^{-1}, the designed reactor has an adequate performance, even at much lower superficial gas velocities.

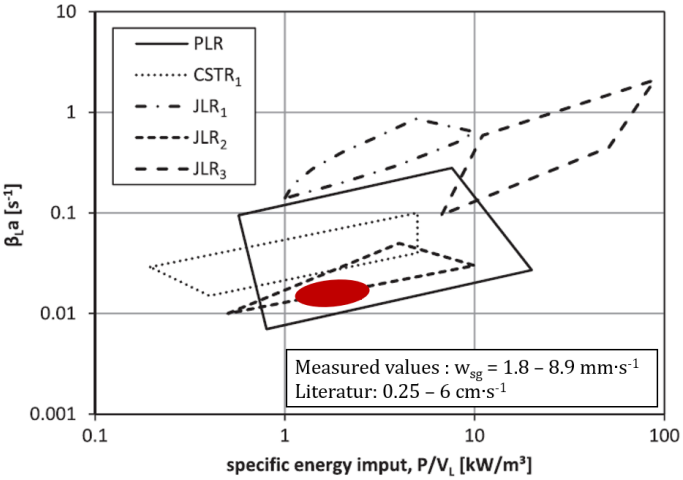

Figure 4-20: Volume specific mass transfer coefficient in dependency of the energy input for different reactor systems, compared to the measured values (red) , based on the diagram proposed by Warnecke [War88]

The stationary measurement of the volume specific mass transfer coefficient allows, besides the estimation of the value itself, the calculation of the transferred mass flux of oxygen. Considering the application as a gassing system, the reactor provides up to 1280 $L \cdot h^{-1}$ oxygen saturated water or transfers an amount of 0.36 $mol \cdot h^{-1}$ of oxygen at standard operating conditions of T = 20°C and p = 1.013 bar.

5 Error Discussion

In the following section the errors of the different measurement campaigns and the resulting calculations are pictured. Besides a qualitative estimation of the different error sources, a quantitative error discussion, either based on the Gaussian propagation of uncertainty or the maximum uncertainty, is done, if possible.

At any time, a value is considered, which was measured more than once, an average over time

$$\bar{x} = \lim_{n\to\infty} \frac{1}{N} \sum_{i=1}^{N} x_i \tag{5.1}$$

and since it is needed for the calculation of the dynamic error, the standard deviation

$$\sigma_x = \sqrt{\sum_{i=1}^{N} \frac{1}{N-1} (x_i - \bar{x})^2} \tag{5.2}$$

is calculated. The dynamic errors are determined by the Gaussian propagation of uncertainty

$$\sigma_z = \sqrt{\sum_{j=1}^{m} \left(\frac{\partial \bar{f}}{\partial x_j} \right) \cdot \sigma_{\bar{x}_j}^2} \tag{5.3}$$

or the maximum error, in case no averaged value is available,

$$\Delta z = \sum_{j=1}^{m} \left| \frac{\partial f}{\partial x_j} \cdot \Delta x_j \right| \tag{5.4}$$

are used. [Bro16]

As the energy dissipation density is containing only the volume flow, which needs to be measured, the error is calculated by knowing the standard deviation and applying the Gaussian propagation of uncertainty

$$\sigma_{P/V} = \sqrt{\sum_{j=1}^{m} \left(\frac{\partial \bar{f}}{\partial V}\right) \cdot \sigma_V^2} \qquad (5.5).$$

The resulting error is listed with the measured values of the energy dissipation density in *Table A- 1*. As the standard deviations of the measured volume fluxes are very small, the dynamic error of the measurement is below 1%.

For all experiments the temperature was controlled by a Julabo W40 thermostat and the temperature was set to 20°C at any time. But the often-changing energy dissipation of the pump and the changing amount of gas inserted into the reactor, caused a temperature fluctuation of about ±0.1 °C. As this degree of fluctuation in temperature is low, it is neglected.

5.1.1 Errors of the Bubble properties

The determination of the bubble properties, as bubble size, interfacial area and gas hold-up, is containing several error sources. The gas hold-up is measured, using a camera and an analyzing tool, which is comparing the actual water level with a target picture, resulting in error sources, while evaluating the target picture and the final water level. As the made error is not known up to this point, the error was estimated to be within a range of ±0.2%. For minimizing the error, the resulting liquid levels are recorded for a period of 120s.

As there is no information about the precision of the fiber optical probe available and the values are analyzed statistically afterwards, the exact error dimension is not known. As an approximation of the error, the standard deviation of the two measurements is taken, resulting in deviations of 0.03 – 1.4 mm for the Sauter diameter. At eight measurements at the cylindrical draft tube, the values are too far apart and unreasonable.

Therefore, only the plausible values are considered. The deviations of these points are approximated to be the mean value of the remaining values, which is equal to 0.6 mm. All information is put together for calculating the error of the interfacial area by applying the maximum error equation

$$\Delta a = \left|\frac{\partial f}{\partial \epsilon_G} \cdot \Delta \epsilon_G\right| + \left|\frac{\partial f}{\partial d_{sa}} \cdot \sigma_{d_{sa}}\right| \tag{5.6}$$

The dynamic errors of the interfacial areas are, due to the big deviations of the Sauter diameters, in a range of 5-25%. In context of the measuring device used and under consideration of the statistical analysis, which is amplifying the error, the error is in a reasonable range.

In contrast, the dynamic error, occurring while determining the bubble size using the camera, is easy to point out and results from measuring the length in the pictures in pixel. Again, the maximum error approach is used for determining the dynamic error. The maximum deviation of measuring the length scale, is approximately ±2px, resulting in an error of ±0.105, while calculating the Sauter diameter.

5.1.2 Dynamic determination of the volumetric mass transfer coefficient

Possible errors in the dynamic determination are caused by the oxygen sensors, the pump circulating the testing volume, the counter diffusion of the dissolved nitrogen and the evaluation method of the data. The specifications and precision of the sensors are listed in *Table 3-3*. The error of the sensors is a systematic and cannot be reduced. The precision, given by the manufacturer, is within a range of ±0.05%. The error, arising from pumping the water into the measuring circuit, is again of systematic nature. As there is gas circulating in the reactor, a small fraction of the gas is entrained into the measuring circuit as well. For minimizing this error, a gas separator is installed directly at the beginning of the measurement section.

For estimating the volume specific mass transfer coefficient, both dynamically and stationary, the saturation concentration of the oxygen is measured, resulting in an error source. The saturation concentration is a time average, measured for 30 minutes. The standard deviation, used for further error estimations, and the maximum and minimum value are listed in *Table 4-1*.

The error, applying the dynamic determination of the volume specific mass transfer coefficient, is strongly depending on the section, which is linearized. In this thesis, the volume specific mass transfer coefficient is evaluated in the range of 20% to 70% of the maximum oxygen saturation. As the error cannot be pointed out exactly, this section was divided in two smaller sections from 20% - 45% and 45% - 70% and the volume specific mass transfer is determined for all three. As a result of splitting up the section and from repeating each measurement, a mean value is calculated, and the maximum and minimum fluctuation is calculated. The determined error is in a range of 15% to 20% and is considered reasonable for this method. The values and the maximum/minimum of each operating point are listed in *Figure A- 4* and *Table A- 5*.

As this method is using nitrogen for evacuating the oxygen from the liquid phase, the counter diffusion of the nitrogen must be considered. The resulting mass flux of nitrogen from the liquid into the gaseous phase is affecting the diffusing oxygen flux and therefore the overall measured volumetric mass transfer coefficient. The resulting error is of systematic nature and cannot be quantified. Though it is important to consider while evaluating the measured data.

5.1.3 Static determination of the mass transfer coefficient

Possible error sources determining the volume specific mass transfer stationary, are caused by the feed flux, which is getting pumped through the reactor, the oxygen sensors and the measurement of the saturation concentration. The feed flux is mainly influenced by the pump and the hydro-

static pressure of the reservoir. The feed flux is recorded during each experiment. A mean value and the standard deviation are used for further calculations. The oxygen concentrations of the inlet and the outlet are as well recorded over time and therefore a mean value over time and the corresponding standard deviation is calculated. As each operating point was measured twice, the mean value is calculated and the minimum/maximum fluctuation is displayed in *Table 4-2* and as error bars in *Figure 4-12*.

For calculating the dynamic error of the transferred oxygen flux, the Gaussian propagation of uncertainty is applied, yielding

$$\sigma_{\dot{n}} = \sqrt{\left(\frac{\partial \bar{f}}{\partial \dot{V}}\right) \cdot \sigma_{\dot{V}}^2 + \left(\frac{\partial \bar{f}}{\partial \rho_{in}}\right) \cdot \sigma_{\rho,i}^2 + \left(\frac{\partial \bar{f}}{\partial \rho_{out}}\right) \cdot \sigma_{\rho,o}^2 + \left(\frac{\partial \bar{f}}{\partial \rho_{max}}\right) \cdot \sigma_{\rho,max}^2} \quad (5.7).$$

The dynamic error for calculating the transferred oxygen flux, is in a range of 15% - 38%. This value seems high, but is affected by several quantities, all adding up to this error.

6 Conclusion and Outlook

The aim of the thesis is the development, commissioning and characterization of a prototype gassing reactor system, providing an optimal mass transfer performance at atmospheric pressure. Therefore, a jet loop reactor is optimized, considering fluid dynamic insights and current literature. A fluid dynamically optimized draft tube, containing drop shaped widenings at both ends, is installed while the annulus space and the cross-sectional area of the riser are equally sized. The optimized approach is then compared to a cylindrical draft tube of the same size and aspect ratios as a benchmark system.

The characterization of both jet loop reactors, the optimized one and the benchmark system, consists of two parts: Determining the gas hold-up and bubble size in the reactor system and evaluating the mass transfer behavior by measuring the volume specific liquid-phase mass transfer coefficient $\beta_L a$. The estimation of the gas hold-up has been carried out in the bachelor thesis of *D. Schnute* and shows that the flow optimization provides an increase of the gas hold-up, especially at lower gassing rates.

Based on the results of the gas hold-up determination, the bubble sizes are measured at different operating conditions. The results show that the flow optimization has not only an impact on the gas hold-up, but also on the bubble sizes, represented by the Sauter diameter and the chord length. The implementation of the flow optimized draft tube, results in larger bubble sizes and therefore, in decreasing specific interfacial areas.

The evaluation of the volume specific mass transfer coefficient is determined, using two different approaches, a dynamic adsorption/desorption method and a stationary method with a constant feed. The results of the dynamic measurements show that the influence of the optimized draft tube on the volume specific mass transfer is negative, when compared to the unmodified draft tube, resulting in a lower mass transfer rate. The stationary measurements are supporting the results of the dynamic method and enables the calculation of the oxygen mass flux. A gassing rate of

$\dot{m}_G = 0.15\ g \cdot s^{-1}$ yields an oxygen flux of $3.2\ mg \cdot s^{-1}$, providing up to $1280\ L \cdot h^{-1}$ of oxygen saturated water.

The measured values are compared to correlations from literature. The first correlation is based on the energy input and the gas flux, proposed by *Farizoglu* [Far07]. The second correlation is a Sherwood correlation proposed by *Jamshidi* [Jam01b], using an adjusted "industrial" Sherwood number. As both correlations are set up for commonly operated jet loop reactors, with much smaller draft tube to reactor ratios, the exponents and constants need to be refitted, resulting in a description of the actual conditions with an error of about ± 10%.

For both draft tubes, the characterized jet loop reactor is providing common mass transfer ability, comparable to literature values [War88]. The flow optimized draft tube results in a higher gas hold-up, since the circulation is intensified. Therefore, this system provides an improvement under some conditions, i.e., if a chemical reaction is consuming a valuable gas.

The interfacial area and therefore the shape and size of the bubbles have a great impact on the mass transfer. Thus, the bubble size- and shape distributions should be an aim of further research, in order to fully understand the processes taking place in the reactor. Also, the volume specific mass transfer coefficient needs to be determined, using the stationary method, at more operating points. Especially, as it is providing the additional information about the transferred oxygen flux.

As the mass transfer of the reactor is not enhanced by the flow optimized draft tube, the draft tube design should be reconsidered. Since sharp edges seem to influence the mass transfer ability of the system, a draft tube which combines the advantages of both designs is suggested.

Since this thesis is part of the BMBF alliance *protP.S.I.,* which is investigating the influence of pressure on a variety of processes, the gained knowledge should be used to design a jet loop reactor system, capable of resisting a high pressure and therefore being able to dissolve more oxy-

gen in water, compared to atmospheric conditions. An idea of the increasing oxygen solubility in water at elevated pressure is displayed in *Figure 6-1*. At a temperature of T = 303 K the amount of soluble oxygen in water is about 170 times higher at 200 bar compared to atmospheric pressure [Gen10]. This indicates the great potential of high pressure processes for biotechnological processes on industrial scales.

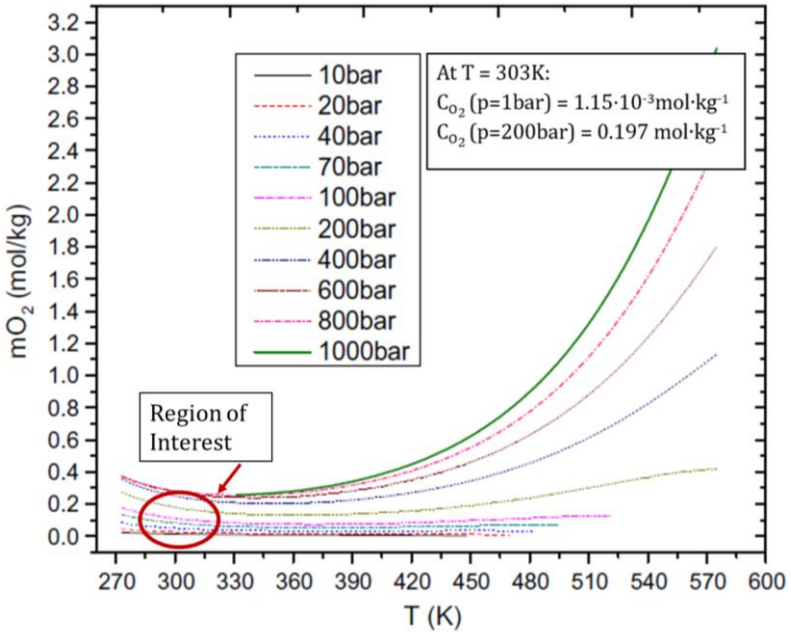

Figure 6-1: Oxygen solubility in pure water for different temperature and pressure ranges [Gen10]

7 Bibliography

[Aki73] Akita, K. et al.: *Gas Holdup and Volumetric Mass Transfer Coefficient in Bubble Columns*, Ind. Eng. Chem. Process Des. Develop., Vol. 12, No. 1, 1973

[Bae16] Baehr, H., Stephan K.: *Wärme-und Stoffübertragung*, Berlin, Heidelberg, Springer-Verlag Berlin Heidelberg, 9th Edit., 2016, ISBN 9783662496763

[Ble65] Blenke, H. et al.: *Beitrag zur optimalen Gestaltung chemischer Reaktoren*, Chemie Ingenieur Technik, 3/1965; p. 10-17

[Ble71] Blenke, H. et al.: *Hydrodynamische Berechnung von Schlaufenreaktoren für Einphasensysteme*, Chemie Ingenieur Technik, 1+2/1971; p. 289-294

[Bra71] Brauer, H.: *Stoffaustausch einschließlich chemischer Reaktionen, Grundlagen der chemischen Technik*, Sauerländer, Aarau/Frankfurt a.M., 1971. ISBN 3794100085

[Bro16] Bronstejn, I., et al.: *Taschenbuch der Mathematik*, Haa-Gruiten Verlag Europa Lehrmittel, 10. Auflage, 2016 ISBN: 3808557907

[Bus17] Busch, C.: *Ermittlung von hydrodynamischen Kenngrößen für die Maßstabsübertragung eines Schlaufenreaktors aus dem Technikums- in den Industriemaßstab*, Masterarbeit, Institut für Mehrphasenströmungen, TUHH, 2017

[Cli78] Clift, R.: *Bubbles, Drops and Patricles*, Academic Press Inc., New York, 1978

[Dae99] Dean, J.A. and Lange, N.A.: *Lange's handbook of chemistry,*McGraw-Hill, New York, 15th ed edn., 1999.

[Far07] Farizoglu, B.: *Influence of draft tube cross-sectional geometry on k_La and ε in jet loop bioreactors (JLB)*, Chemical Engineering Journal, 133/2007, p. 293-299

[Gla77] Glaeser, H., Brauer, H.: *Berechnung des Impuls- und Stofftransportes durch die Grenzfläche einer formveränderlichen Blase*, VDI-Forschungsheft 581, Verein Deutscher Ingenieure Verlag, Düsseldorf, 1977

[Gen10] Geng, M.: Prediction of oxygen solubility in pure water and brines up to high temperatures and pressures, Geochimica et Cosmochimica Acta, 74/2010, p5631-5640

[Gra76] Grace, J.: *Shapes and velocities of single drops and bubbles moving freely through immiscible liquids*, Transact. Inst. Chem. Eng. 54/1976 p. 167

[Jam01a] Jamshidi, A., et al.: *Studies on the hydrodynamic behavior and mass transfer in a down-flow jet loop reactor with a coaxial draft tube*, Journal of Chemical Technology and Biotechnology, 76/2001, p. 39-46

[Jam01b] Jamshidi, A., et al.: *Hydrodynamic and mass transfer characterization of down flow jet loop bioreactor*, Biochemical Engineering Journal, 8/2001, p. 241-250

[Kra12] Kraume, M.: *Transportvorgänge in der Verfahrenstechnik: Grundlagen und apparative Umsetzungen*. Springer Berlin Heidelberg, Berlin, Heidelberg, 2. edit., 2012. ISBN 9783642251481.

[Liu98] Liu, W., Clark, N.: *Relationship between bubble size distributions and chord-length distribution in heterogeneously bubbling systems*, Chemical Engineering Science, 53/1998, pages 1267-1276

[Loh90] Lohrengel, B.: *Untersuchung zur Fluiddynamik zwei- und dreiphasig betriebener Schlaufenreaktoren*, Dissertation, Universität Clausthal, 1990

[Mer77] Mersmann, A.: *Auslegung und Maßstabsvergrößerung von Blasen- und Tropfensäulen*, Chemie Ingenieur Technik, 9/1977; p. 679 -770

[Mer86] Mersmann, A.: *Stofftransport*, Berlin, Springer, 1986, ISBN 3540159207.

[Nak80] Nakanoh, M. and Yoshida, F.: *Gas Adsorption by Newtonian and Non-Newtonian Liquids in a Bubble Column*, Ind. Eng. Chem. Process Des- Dev., 19/1980, p. 190-195

[Pas04] Paschedag A.: *CFD in der Verfahrenstechnik*, Weinheim, Wiley-VCH Verlag GmbH & Co. KGaA, 2004

[Pre19] Website Presens Precision Sensing, *Messprinzip chemisch-optischer Sensoren,* last excessed on 20.02.2019 *https://www.presens.de/de/wissen/grundlagen/detail/messprinzip-chemisch-optischer-sensoren-1554.html*

[Oer15] Oertel, H., Böhle M., Reviol T. *Strömungsmechanik*. 7. edit. Wiesbaden: Springer Vieweg, 2015

[Rae83] Räbiger, N., Vogelpohl, A.: *Der Kompaktreaktor, ein neuentwickelter Schlaufenreaktor mit hoher Stoffaustauschleistung*, Chemie Ingenieur Technik, 6/1983; p. 486-487

[Rae88] Räbiger, N.: *Hydrodynamik und Stoffaustausch in strahlgetriebenen Schlaufenreaktoren*, Köln, Verlag TÜV Rheinland GmbH, 1988

[Sch19] Schnute, D.: *Optimierungspotenzial von Treibstrahl-Schlaufenreaktoren durch 3D-gedruckte Einbauten*, Bachelorarbeit, Institut für Mehrphasenströmung, TUHH, 2019

[Vdi13a] Verein Deutscher Ingenieure, Gesellschaft Verfahrenstechnik und Chemieingenieurwesen. *VDI-Wärmeatlas, Chapter A,* 11 edit. Berlin [u.a.]: Springer Vieweg,2013

[Vdi13b] Verein Deutscher Ingenieure, Gesellschaft Verfahrenstechnik und Chemieingenieurwesen. *VDI-Wärmeatlas, Chapter L4.1,* 11 edit. Berlin [u.a.]: Springer Vieweg,2013

[Vog87] Vogelpohl, A., Wachsmann, U.: *Zur Hydrodynamik von strahlgetriebenen Schlaufenreaktoren*, Chemie Ingenieur Technik, 6/1987; p. 510-511

[Wac85] Wachsmann, U. et al.: *Einfluss der Geometrie auf die Hydrodynamik und den Stoffaustausch im Kompaktreaktor*, Chemie Ingenieur Technik, 4/1985; p. 346-347

[Wac86] Wachsmann, U.: *Zur Hydrodynamik strahlgetriebener Schlaufenreaktoren*, Dissertation, Universität Clausthal, 1986

[War16] Warmeling, H. et al.: *Jet loop reactors as a versatile reactor set up – Intensifying catalytic reactions: A review*, Chemical Engineering Science, 149/2106, p. 229-248

[War88] Warnecke, H. et al.: *Mass Transfer of Gas-Liquid Jet Loop Reactors*, Chem. Eng. Technol., 11/1988, p. 306-311

[Wie11] Wiedemann, M. *Einfluss der lokalen Energiedissipationsdichte in Reaktoren auf Umsatz und Selektivität Chemischer Reaktionen*, Dissertation, Univ. Bremen, 2011

[Zeh05] Zehner, P., Kraume, M.: *Ullmann's Encyclopedia of Industrial Chemistry*: *Bubble Columns*, Weinheim, Wiley-VCH Verlag, 2005

[Zua13] Zuanon, N.: *B-POP: Phase detection optical probe for bubbly flows - User Manual*, Grenoble, France, A2 Photonics Sensors, 05/2013

A Appendix

Table A- 1: Energy dissipation densities of the different reactors including the corresponding errors

Draft tube Type (A)		***Draft tube Type (B)***	
Mean Energy Dissipation P/V / kW·m^{-3}	***Deviation / %***	***Mean Energy Dissipation P/V / kW·m^{-3}***	***Deviation / %***
2,10	± 0,038%	2,07	± 0,036%
2,56	± 0,046%	2,49	± 0,038%
2,98	± 0,183%	2,92	± 0,035%
3,47	± 0,050%	3,41	± 0,035%
4,08	± 0,047%	4,03	± 0,032%
4,56	± 0,062%	4,49	± 0,036%
4,82	± 0,040%	4,74	± 0,042%

Table A- 2: Bubble size data used in Figure 4-6 obtained with the fiber optical probe, statistically analyzed by the correlation of Liu & Clark and the High-Speed cam

Superficial gas velocity $w_{g,0}$ /mm·s^{-1}-	***A2-Photonics Probe d_{sa} / mm***	***Correlation Liu & Clark d_{sa} / mm***	***High Speed Cam d_{sa} / mm***
1.8	2,46	4,86	5,97
	2,79	5,53	5,24
	2,67	5,28	5,68
	2,64	5,28	5,77
	2,43	4,83	5,43
	2,43	5,17	5,24
	1,93	4,12	5,85
3.6	2,50	5,08	6,13
	2,02	4,05	5,93
	2,19	4,37	5,70
	2,29	4,66	5,40
	2,20	4,55	5,45
5.3	3,02	5,90	6,66
	2,90	5,97	5,90
	2,52	5,34	6,01
8.9	2,25	5,12	6,85
	2,01	4,54	6,60

Table A- 3: Results of the dynamic volume specific mass transfer coefficient determination applying the cylindrical draft tube

Superficial gas velocity $w_{g,0}$ ***/mm·s^{-1}-***	***Volumetric mass transfer coefficient*** $\beta_L a$***/ s^{-1}***	***Negative Deviation - /%***	***Positive Deviation - /%$^{-1}$***
1.8	49,89	12,92	12,27
	52,14	14,65	13,33
	52,80	15,29	13,36
	52,22	14,40	14,19
	52,38	13,82	12,27
	51,23	12,90	11,70
	51,64	14,04	11,01
3.6	64,46	11,50	9,45
	66,31	12,21	9,93
	68,38	12,70	11,24
	68,39	14,64	14,29
	70,14	15,00	13,33
5.3	73,16	12,65	9,87
	73,57	15,77	13,74
	73,87	14,36	12,68
8.9	79,23	11,72	11,36
	79,68	13,75	14,61

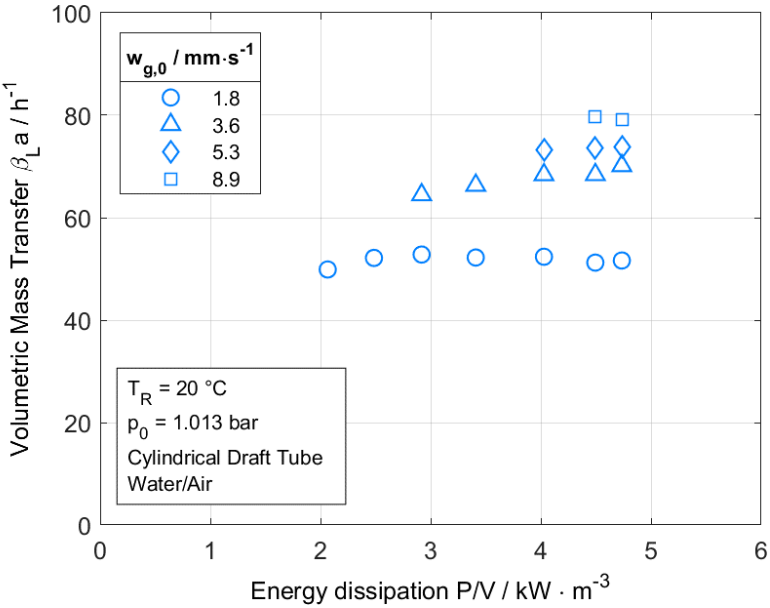

Figure A- 4: Measured data points of the cylindrical draft tube (light blue)

Table A- 5: Results of the dynamic volume specific mass transfer coefficient determination applying the flow optimized draft tube

Superficial gas velocity $w_{g,0}$ /mm·s^{-1}-	***Volumetric mass transfer coefficient $\beta_L a$/ s^{-1}***	***Negative Deviation - /%***	***Positive Deviation - /%$^{-1}$***
1.8	51,65	14,65	13,65
	49,26	18,08	18,16
	50,46	16,23	15,73
	50,70	19,74	20,93
	51,31	16,91	16,16
	52,35	14,59	13,46
	53,99	16,36	14,06
3.6	57,62	14,69	13,97
	56,27	13,01	10,63
	60,76	15,86	16,64
	61,10	14,41	18,24
	58,71	19,44	20,26
5.3	69,38	11,93	10,29
	74,62	17,24	16,05
	74,40	17,03	17,47
8.9	91,92	10,47	10,95
	90,17	16,68	15,26

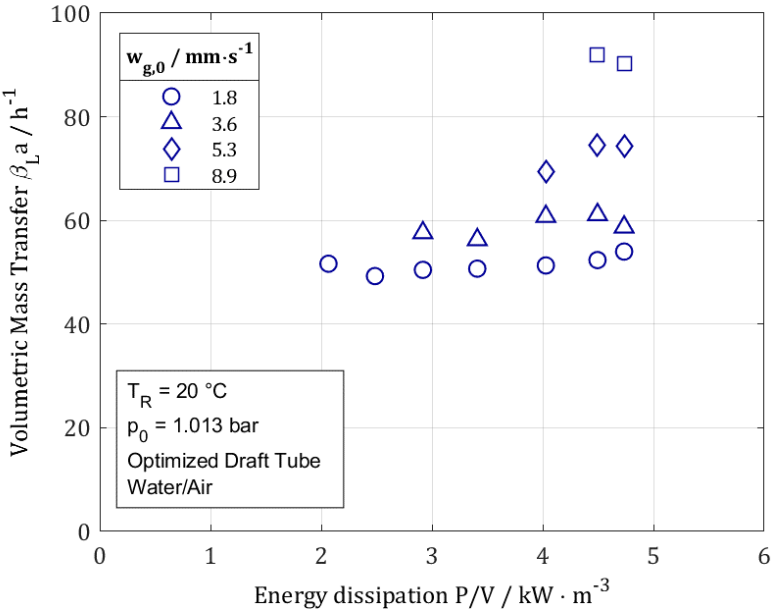

Figure A- 6: Measured data points of the flow optimized draft tube (dark blue)

Table A- 7: Measured specific interfacial areas for both draft tubes. Bubble size information are based on the statistical analysis of Liu & Clark

Superficial gas velocity $w_{g,0}$ ***/mm·s⁻¹***	***Cylindric Draft Tube***		***Optimized Draft Tube***	
-	***Area*** a ***/m⁻¹***	***Deviation - /%***	***Area*** a ***/m⁻¹***	***Deviation - /%***
1.8	44.48	23.13	44.38	20.52
	39.03	25.47	51.28	11.42
	40.04	15.78	53.05	11.07
	39.53	17.14	55,19	7
	41.5	16.99	52.64	7.46
	38.69	11.9	51.93	12.82
	48.47	15.04	57.77	24.08
3.6	82.89	14.67	63.18	14.55
	107.46	17.55	68.11	22.91
	102.41	16.42	75.20	15.25
	98.49	15.48	76.34	23.80
	101.54	15.78	66.56	19.45
5.3	89.62	12.43	66.97	16.46
	91.65	12.24	73.97	14.22
	105.17	13.37	74.28	13.90
8.9	129.9	7.63	94.03	10.75
	151.13	18.44	105.53	5.78

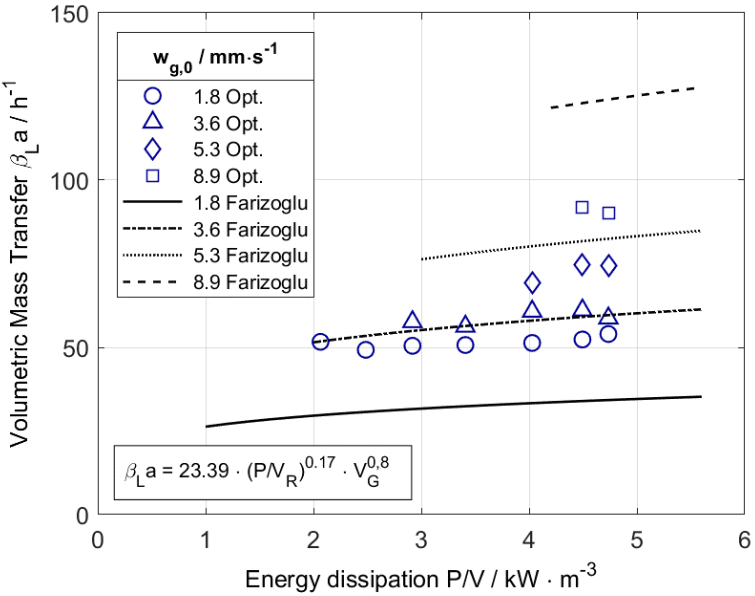

Figure A- 8*: Measured data points of the flow optimized draft tube (dark blue), compared to the correlated values by Farizoglu (black)*

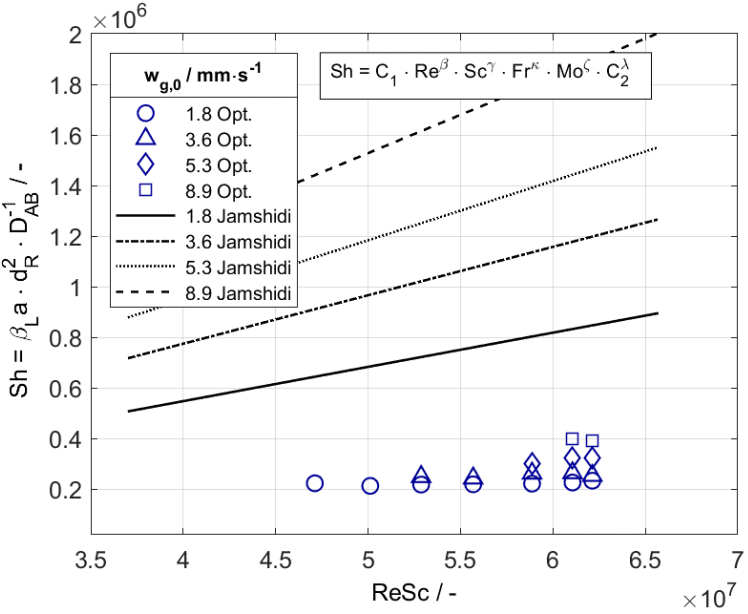

Figure A- 9: Industrial Sherwood number in dependency of (ReSc) for four different gassing rates (grey), compared to the measured values, applying the flow optimized draft tube (dark blue)

This Matlab code is based on the work of Liu & Clark who proposed a statistical analysis for transforming chord length information into bubble size information:

```
%% number of bins

numberOfBins=40;
ymax=max(Y);
deltay=ymax/numberOfBins;
if nargin==1
   alpha=1;
end

Rmax=ymax/2/alpha;
deltaR=Rmax/numberOfBins;
y=((1:numberOfBins)-.5)*deltay;
R=((1:numberOfBins)-.5)*deltaR;
h=sqrt(mean(Y)-std(Y))/length(Y)^(.2);



%% Vector containing the probability of chord length

W=zeros(numberOfBins,1);
for i=1:numberOfBins-1
   numberOfOccurancesInInterval=0;
   for j=1:length(Y)
      numberOfOccurancesInInterval=numberOfOccurancesInInter-
val+(Y(j)>y(i) && Y(j)<=y(i+1));
   end
   W(i)=numberOfOccurancesInInterval/length(Y);
End
```

```
%% Right hand side P_ce/deltaR

P_ce=zeros(numberOfBins,1);
for i=1:numberOfBins
   for j=1:length(Y)
      P_ce(i)=P_ce(i)+exp(-(y(i)-Y(j))^2/2/h/h);
   end
   P_ce(i)=P_ce(i)/length(Y)/h/sqrt(2*pi);
end



%% Matrix E

P_Ry=@(y,R) y*exp(y*y/4/alpha/alpha-R*R)/2/alpha/alpha/(1-exp(-
R*R));
E=zeros(numberOfBins);
for i=1:numberOfBins
   E(i,i)=1/2*P_Ry(y(i),R(i));
   for j=(i+1):numberOfBins
      E(i,j)=P_Ry(y(i),R(j));
   end
end



%% Solve for the propability density function



P_p=(E\(P_ce./deltaR));
fprintf('assure %f is approximately equal to one\n',trapz(R,P_p))
P_abs=zeros(1,numberOfBins);
```

```
%% Probablity density function

P_abs(1)=P_p(1)/2*deltaR;
for i=2:numberOfBins
   P_abs(i)=(P_p(i-1)+P_p(i))/2*deltaR;
end



%% Q3 Distribution

M30=sum(R.*R.*R.*P_abs*16*deltaR);
q3=16/M30*R.*R.*R.*P_abs;

%% Mean Sauter diameter

Vges=0;
Sges=0;
for i=1:numberOfBins
   Sges=Sges+P_p(i)*4*pi*R(i)*R(i);
   Vges=Vges+P_p(i)*4/3*pi*R(i)*R(i)*R(i);
end

d32=6*Vges/Sges;
fprintf('sauter diameter %f [mm]\n',d32)
```